

An unfitted high-order HDG method for two-fluid Stokes flow with exact NURBS geometries

Stefano Piccardo^{1,3,4}, Matteo Giacomini^{1,2,*} and Antonio Huerta^{1,2}

Abstract

A high-order, degree-adaptive hybridizable discontinuous Galerkin (HDG) method is presented for two-fluid incompressible Stokes flows, with boundaries and interfaces described using NURBS. The NURBS curves are embedded in a fixed Cartesian grid, yielding an unfitted HDG scheme capable of treating the exact geometry of the boundaries/interfaces, circumventing the need for fitted, high-order, curved meshes. The framework of the NURBS-enhanced finite element method (NEFEM) is employed for accurate quadrature along immersed NURBS and in elements cut by NURBS curves. A Nitsche's formulation is used to enforce Dirichlet conditions on embedded surfaces, yielding unknowns only on the mesh skeleton as in standard HDG, without introducing any additional degree of freedom on non-matching boundaries/interfaces. The resulting unfitted HDG-NEFEM method combines non-conforming meshes, exact NURBS geometry and high-order approximations to provide high-fidelity results on coarse meshes, independent of the geometric features of the domain. Numerical examples illustrate the optimal accuracy and robustness of the method, even in the presence of badly cut cells or faces, and its suitability to simulate microfluidic systems from CAD geometries.

Keywords: Hybridizable discontinuous Galerkin, Unfitted meshes, Exact NURBS geometry, Stokes flows, High-order, Immiscible fluids.

¹Laboratori de Càlcul Numèric (LaCàN), ETS de Ingeniería de Caminos, Canales y Puertos, Universitat Politècnica de Catalunya, Barcelona, Spain.

²Centre Internacional de Mètodes Numèrics en Enginyeria (CIMNE), Barcelona, Spain.

³CERMICS, Ecole des Ponts, 77455 Marne-la-Vallée, France.

⁴INRIA, 2 rue Simone Iff, 75589 Paris, France.

* Corresponding author: Matteo Giacomini. *E-mail:* matteo.giacomini@upc.edu

1 Introduction

The simulation of multi-fluid systems and multi-phase flows entails a series of numerical challenges related to the different flow features that may arise from the interaction of different materials and phases [1–3]. In this context, high-order methods [4] have received increasing attention in recent years, given their suitability to devise high-fidelity solvers for complex flow problems [5, 6].

Despite their proven superiority in terms of accuracy and computational efficiency [7–9], the adoption of high-order methods (e.g., discontinuous Galerkin –DG–) is still limited outside of the academic environment, mainly due to their reduced robustness with respect to low-order methods and the challenges to automatically generate high-order, curved meshes. The latter issue is particularly critical since the error introduced by the geometric approximation of a computer aided design (CAD) model can be responsible for the appearance of non-physical effects in the numerical solution, as reported in the literature [10, 11]. To remedy this issue, the NURBS-enhanced finite element method (NEFEM) was proposed in [12, 13], offering a seamless integration of the standard finite element method (FEM) with a CAD representation of the boundary during simulation. Whilst NEFEM provides a flexible computing environment, allowing for a simple treatment of trimmed and degenerate NURBS, without the need for complex, manual de-featuring procedures, the automatic generation of meshes suitable for NEFEM represents an open field of investigation, with some promising recent contributions [14, 15].

An alternative approach to ease the difficulties of geometry treatment is represented by immersed boundary methods [16]. Many *unfitted*, *embedded* or *immersed* methods have been proposed in the literature, spanning the unfitted finite element method [17] coupled with Nitsche’s method [18, 19], the fictitious domain method [20, 21], the cutFEM [22–24] and cutDG [25] methods, the finite cell method [26], the aggregated FEM [27] and the shifted boundary method [28]. It is well known that unfitted methods tend to suffer in the presence of small cuts in the mesh, possibly leading to ill-conditioned systems [29]. To remedy this issue, several techniques have been proposed in the literature, including ghost penalty [30], cell agglomeration [31] and element extension [32]. For a detailed discussion about these topics, interested readers are referred to [33, 34].

Whilst well-established for low-order functional and geometric approximations, unfitted methods have been less studied in a high-order context featuring exact geometry. Extensions towards high order have been proposed for the finite cell method [35], the unfitted FEM using high-order geometrical maps [36] and the unfitted DG method with cell agglomeration [37]. More recently, high-order versions were presented for ghost penalty [38], shifted boundary method [39] and aggregated FEM [40]. Concerning exact geometry treatment, unfitted approaches employing B-Splines and NURBS were discussed in [41, 42] using the finite cell method, in [43] via NEFEM, in [44, 45] based on the immersogeometric framework and in [32, 46] for the Cartesian grid FEM and DG methods.

The goal of this work is to devise an unfitted method merging the advantages of high-

order functional approximations and exact treatment of the NURBS geometry. Stemming from the high-order hybridizable discontinuous Galerkin (HDG) rationale proposed in [47], a high-fidelity solver is devised for Stokes flows featuring immersed boundaries, as well as interface problems with two fluids. Owing to the hybridization procedure, this allows to significantly reduce the globally coupled degrees of freedom of the problem, eliminating all element-based unknowns [8]. In this work, boundaries and interfaces are represented exactly by means of NURBS [48], which are incorporated in the HDG solver via the NEFEM paradigm [49]. The main novelties of the proposed approach are: (i) the flexibility of treating exact NURBS geometry within non-matching grids, thus eliminating the difficulties of high-order mesh generation; (ii) the suitability of HDG to construct high-order approximations with immersed boundaries, without the need to introduce additional unknowns along the contours/interfaces; (iii) the capability of devising a degree-adaptive procedure, exploiting the exact representation of the geometry via NEFEM and the superconvergent properties of the HDG primal variable. The resulting unfitted high-order HDG-NEFEM method has close connections with other techniques proposed in recent years. Whilst it shares the definition of face unknowns with the unfitted HDG method [50], the extended HDG method [51, 52], the hybridized cutFEM [53] and the unfitted hybrid high order method [54–57], the uniqueness of the proposed approach lies in the definition of unfitted exact geometries via NURBS. Moreover, this work inherits from [32] the element extension strategy employed to handle badly cut cells, whereas, differently from it, it exploits hybridization to reduce the number of globally coupled degrees of freedom in the system.

The rest of this article is organized as follows. After introducing the two-fluid Stokes interface problem in Section 2, Section 3 describes the unfitted HDG formulation, accounting for both immersed boundaries and immersed interfaces, and a degree-adaptive procedure. In section 4, technical details are discussed concerning the treatment of unfitted interfaces, the NEFEM numerical quadrature in the presence of elements cut by NURBS and the element extension strategy to handle badly cut cells. The numerical results are reported in Section 5: the robustness and accuracy of the method are assessed by means of a series of benchmarks with unfitted boundaries and unfitted interfaces and two applications to microfluidic systems. Finally, Section 6 summarizes the results of this work and two appendices provide technical details for the use of NURBS in the presented unfitted HDG-NEFEM framework.

2 Problem statement

Let $\Omega \subset \mathbb{R}^{n_{sd}}$ be an open bounded domain with boundary $\partial\Omega$ and $n_{sd} = 2$ be the number of spatial dimensions. The boundary $\partial\Omega$ is composed of two disjoint parts, the Dirichlet portion Γ_D , and the Neumann portion Γ_N . Formally, $\partial\Omega = \overline{\Gamma_D} \cup \overline{\Gamma_N}$ such that $\Gamma_D \cap \Gamma_N = \emptyset$.

Suppose also that Ω is split by a fixed interface Υ into two disjoint subdomains, each occupied by an immiscible incompressible Stokes fluid. That is, $\overline{\Omega} = \overline{\Omega^1} \cup \overline{\Omega^2}$, $\Omega^1 \cap \Omega^2 = \emptyset$,

and $\Upsilon = \overline{\Omega^1} \cap \overline{\Omega^2}$. Note that, for each fluid, the boundary is $\partial\Omega^i = \Gamma_D^i \cup \Gamma_N^i \cup \Upsilon$ with $\Gamma_D^i \cap \Upsilon = \emptyset$, and $\Gamma_N^i \cap \Upsilon = \emptyset$, for $i = 1, 2$. Moreover, define the domain $\hat{\Omega}$ as $\hat{\Omega} := \Omega^1 \cup \Omega^2$ and, similarly, $\hat{\Gamma}_D := \Gamma_D^1 \cup \Gamma_D^2$ and $\hat{\Gamma}_N := \Gamma_N^1 \cup \Gamma_N^2$. The interface Υ and the boundary $\partial\Omega$ are represented using NURBS and are composed by \mathbf{n}_Υ and $\mathbf{n}_{\partial\Omega}$ NURBS curves, respectively. That is,

$$\Upsilon := \bigcup_{j=1}^{\mathbf{n}_\Upsilon} \mathbf{C}_\Upsilon^j([0, 1]), \quad \partial\Omega := \bigcup_{j=1}^{\mathbf{n}_{\partial\Omega}} \mathbf{C}_{\partial\Omega}^j([0, 1]), \quad (1)$$

where $\mathbf{C}_\diamond^j : \lambda \mapsto \mathbf{C}_\diamond^j(\lambda)$ is a generic NURBS curve [48, 58] defined in the parametric domain $\lambda \in [0, 1]$.

The problem aims to find the unknown velocity and pressure fields, $(\mathbf{u}, p) \in [\mathcal{H}^1(\hat{\Omega})]^{\mathbf{n}_{\text{sd}}} \times \mathcal{L}^2(\hat{\Omega})$, whose restrictions to each subdomain Ω^i are $(\mathbf{u}, p)|_{\Omega^i} = (\mathbf{u}^i, p^i) \in [\mathcal{H}^1(\Omega^i)]^{\mathbf{n}_{\text{sd}}} \times \mathcal{L}^2(\Omega^i)$, $i = 1, 2$, and where $[\mathcal{H}^1(\hat{\Omega})]^{\mathbf{n}_{\text{sd}}} := \{\mathbf{v} \in [\mathcal{L}^2(\hat{\Omega})]^{\mathbf{n}_{\text{sd}}} \mid \mathbf{v}|_{\Omega^i} \in [\mathcal{H}^1(\Omega^i)]^{\mathbf{n}_{\text{sd}}}, \forall i = 1, 2\}$. Given the velocity profile $\mathbf{u}_D \in [\mathcal{H}^{\frac{1}{2}}(\hat{\Gamma}_D)]^{\mathbf{n}_{\text{sd}}}$ imposed on the Dirichlet portion of the boundary and the Neumann datum $\mathbf{t} \in [\mathcal{L}^2(\hat{\Gamma}_N)]^{\mathbf{n}_{\text{sd}}}$ applied on $\hat{\Gamma}_N$, the strong form of the problem can be written as find $(\mathbf{u}, p) \in [\mathcal{H}^1(\hat{\Omega})]^{\mathbf{n}_{\text{sd}}} \times \mathcal{L}^2(\hat{\Omega})$ such that

$$\left\{ \begin{array}{ll} -\nabla \cdot (\mu \nabla \mathbf{u} - p \mathbf{I}_{\mathbf{n}_{\text{sd}}}) = \mathbf{s} & \text{in } \hat{\Omega}, \\ \nabla \cdot \mathbf{u} = 0 & \text{in } \hat{\Omega}, \\ \mathbf{u} = \mathbf{u}_D & \text{on } \hat{\Gamma}_D, \\ (\mu \nabla \mathbf{u} - p \mathbf{I}_{\mathbf{n}_{\text{sd}}}) \mathbf{n} = \mathbf{t} & \text{on } \hat{\Gamma}_N, \end{array} \right. \quad (2)$$

$$\left\{ \begin{array}{ll} \mathbf{u}^1 = \mathbf{u}^2 \\ [(\mu \nabla \mathbf{u} - p \mathbf{I}_{\mathbf{n}_{\text{sd}}}) \mathbf{n}] = \gamma (\nabla \cdot \mathbf{n}^1) \mathbf{n}^1 - (\mathbf{I}_{\mathbf{n}_{\text{sd}}} - \mathbf{n}^1 \otimes \mathbf{n}^1) \nabla \gamma & \text{on } \Upsilon, \end{array} \right.$$

where $\mu = \mu^i > 0$ in Ω^i , $i = 1, 2$, is the piecewise dynamic viscosity of each fluid, assumed constant in Ω^i , $\mathbf{s} \in [\mathcal{L}^2(\hat{\Omega})]^{\mathbf{n}_{\text{sd}}}$ is the volumetric source term, \mathbf{n}^i is the unit normal vector exiting domain Ω^i , and γ is the surface tension coefficient. Finally, the last two equations impose the continuity of velocity and equilibrium of forces along the interface Υ .

Note also the use of the *jump* operator, $[[\odot]]$, which follows the definition introduced in [59]. Along any $(\mathbf{n}_{\text{sd}}-1)$ -dimensional manifold the *jump* operator sums the values of a generic quantity \odot from the left and from the right, namely,

$$[[\odot]] := \odot_l + \odot_r, \quad (3)$$

in this case, since the discontinuity is along Υ , then $l=1$ and $r=2$ or viceversa. Note that the above definition of the jump operator always involves the outward unit normal to a surface.

Remark 1 [Surface tension] Note that in the last equation in (2) the choice of \mathbf{n}^1 in the right-hand-side of the equation is arbitrary because

$$\gamma (\nabla \cdot \mathbf{n}^1) \mathbf{n}^1 - (\mathbf{I}_{\mathbf{n}_{\text{sd}}} - \mathbf{n}^1 \otimes \mathbf{n}^1) \nabla \gamma = \gamma (\nabla \cdot \mathbf{n}^2) \mathbf{n}^2 - (\mathbf{I}_{\mathbf{n}_{\text{sd}}} - \mathbf{n}^2 \otimes \mathbf{n}^2) \nabla \gamma.$$

Moreover, in most cases, the surface tension, γ , is assumed constant, thus, $\nabla\gamma = \mathbf{0}$, and, consequently, the interface shear stress is continuous. Without loss of generality, this assumption is retained in the rest of the paper.

Remark 2 [One-fluid problem] When $\Upsilon = \emptyset$, the interface conditions disappear, and one-fluid problem is solved in domain $\Omega^1 \equiv \Omega$.

Remark 3 [Uniqueness of pressure] When $\hat{\Gamma}_N = \emptyset$, the Stokes interface problem is solvable up to a global additive constant on the pressure, which we fix by imposing

$$\int_{\hat{\Omega}} p \, d\hat{\Omega} = \int_{\hat{\Omega}} p^{\text{ref}} \, d\hat{\Omega},$$

where p^{ref} is a reference pressure value, typically equal to zero. Instead of imposing an average pressure reference, it is also usual to prescribe the pressure at one point.

Remark 4 [Multi-fluid interface problem] Formulation (2) can be readily extended to address multi-fluid problems, where Ω is partitioned into a generic number of connected, open, bounded sets, each occupied by an immiscible, incompressible Stokes fluid.

3 Unfitted HDG formulation

Let Ω_o be a shape-regular polyhedral domain containing Ω , i.e., $\Omega \subseteq \Omega_o$. Then, consider a shape-regular mesh composed of \mathbf{n}_{e1} disjoint (open) subdomains Ω_e such that Ω_o is exactly covered, i.e.,

$$\overline{\Omega_o} := \bigcup_{e=1}^{\mathbf{n}_{e1}} \overline{\Omega_e}.$$

The boundaries $\partial\Omega_e$ of the mesh element Ω_e define the *internal skeleton*, Γ , as

$$\Gamma := \left[\bigcup_{e=1}^{\mathbf{n}_{e1}} \partial\Omega_e \right] \setminus (\hat{\Gamma}_D \cup \hat{\Gamma}_N \cup \partial\Omega_o).$$

We denote by Γ_f a generic internal face of Γ , and by \mathbf{n}_{fc} the total number of internal faces, i.e., $\Gamma = \bigcup_{f=1}^{\mathbf{n}_{fc}} \Gamma_f$. It is important to recall that the interface, Υ , and the external boundary, $\hat{\Gamma}_D$ and $\hat{\Gamma}_N$, do not need to align with the mesh. Moreover, for all $e = 1, \dots, \mathbf{n}_{e1}$, define Ω_e^i the region of Ω_e that belongs to the fluid indexed by i , that is,

$$\Omega_e^i := \Omega_e \cap \Omega^i, \quad \forall i = 1, 2.$$

Similarly, define $\partial\Omega_e^i := \partial\Omega_e \cap (\overline{\Omega^i} \setminus \Upsilon)$ as the portion of the boundary $\partial\Omega_e$ belonging to fluid i .

On this broken domain, problem (2) can be written in mixed form as follows:

$$\left\{ \begin{array}{ll} \mathbf{L}_e^i + \sqrt{\mu^i} \nabla \mathbf{u}_e^i = \mathbf{0} & \text{in } \Omega_e^i, \\ \nabla \cdot (\sqrt{\mu^i} \mathbf{L}_e^i) + \nabla p_e^i = \mathbf{s} & \text{in } \Omega_e^i, \\ \nabla \cdot \mathbf{u}_e^i = 0 & \text{in } \Omega_e^i, \\ \mathbf{u}_e^i = \mathbf{u}_D & \text{on } \Gamma_D^i \cap \overline{\Omega}_e, \\ (\sqrt{\mu^i} \mathbf{L}_e^i + p_e^i \mathbf{I}_{\text{nsd}}) \mathbf{n}_e^i = -\mathbf{t} & \text{on } \Gamma_N^i \cap \overline{\Omega}_e, \end{array} \right. \quad \text{for } e = 1, \dots, \mathbf{n}_{e1} \text{ and } i = 1, 2, \quad (4a)$$

$$\left\{ \begin{array}{l} \mathbf{u}_e^1 = \mathbf{u}_e^2 \\ \llbracket (\sqrt{\mu} \mathbf{L}_e + p_e \mathbf{I}_{\text{nsd}}) \mathbf{n}_e \rrbracket = -\gamma (\nabla \cdot \mathbf{n}_e^1) \mathbf{n}_e^1 \end{array} \right. \quad \text{on } \Upsilon \cap \Omega_e, \quad \text{for } e = 1, \dots, \mathbf{n}_{e1}, \quad (4b)$$

$$\left\{ \begin{array}{l} \llbracket \mathbf{u}^i \otimes \mathbf{n}^i \rrbracket = \mathbf{0} \\ \llbracket (\sqrt{\mu^i} \mathbf{L}^i + p^i \mathbf{I}_{\text{nsd}}) \mathbf{n}^i \rrbracket = \mathbf{0} \end{array} \right. \quad \text{on } \Gamma \cap \Omega^i, \quad \text{for } i = 1, 2, \quad (4c)$$

where $\mathbf{L} := -\sqrt{\mu} \nabla \mathbf{u}$ is the mixed variable so that $\mathbf{L}_e^i = -\sqrt{\mu^i} \nabla \mathbf{u}_e^i$ is its restriction to Ω_e^i , for $e = 1, \dots, \mathbf{n}_{e1}$ and $i = 1, 2$. Note that the *jump* operator acts over the interface, Υ , in (4b) whereas this operator acts along $\Gamma \cap \Omega^i$ for $i = 1, 2$ in (4c).

The interface conditions stated in (4b) are those presented in (2), rewritten element-by-element to ensure the enforcement of the desired continuity conditions.

Equations (4a) and (4c) are, respectively, the so-called *local problems* and *transmission conditions* common in HDG, see [60]. It is worth noting that here, following [61], the HDG formulation imposes the Neumann boundary condition in the local problem instead of the global one as it is usually done in HDG. This leads to a marginally smaller discrete global problem but, more importantly, avoids the definition of hybrid unknowns along the Neumann boundary (regardless of having a fitted or unfitted Neumann boundary). The transmission conditions impose, respectively, continuity of velocity and normal flux across the skeleton of the mesh. Finally, in order to solve the local problems, HDG methods introduce the so-called *hybrid velocity*: this is a face-based variable $\hat{\mathbf{u}}^i$ that represents the trace of the solution on each face of $\Gamma \cap \Omega^i$ so that each local (element-by-element) problem described by (4a) is completed by adding

$$\mathbf{u}_e^i = \hat{\mathbf{u}}^i \quad \text{on } \Gamma \cap \partial \Omega_e^i, \quad \text{for } e = 1, \dots, \mathbf{n}_{e1} \text{ and } i = 1, 2. \quad (5)$$

To simplify the presentation, consider three types of elements: (i) *standard HDG elements*, which are those not cut by Υ or $\partial \Omega$, that is, $\Upsilon \cap \Omega_e = \emptyset$ and $\partial \Omega \cap \Omega_e = \emptyset$; (ii) *immersed boundary elements* cut by $\partial \Omega$ but not by Υ , that is, $\Upsilon \cap \Omega_e = \emptyset$ and $\partial \Omega \cap \Omega_e \neq \emptyset$; and (iii) *interface elements* cut by Υ but not by $\partial \Omega$, that is, $\Upsilon \cap \Omega_e \neq \emptyset$ and $\partial \Omega \cap \Omega_e = \emptyset$. For the sake of readability, the method is presented assuming that the interface splits each element (at most) into two different regions. Figure 1 illustrates a possible configuration and the extension to the case of multiple subregions is commented in Appendix A. Finally, note that all the defined elements, (i), (ii), and (iii), also encompass the case in which the external boundary is aligned with the mesh skeleton, which means $\partial \Omega_e \cap \partial \Omega \neq \emptyset$.

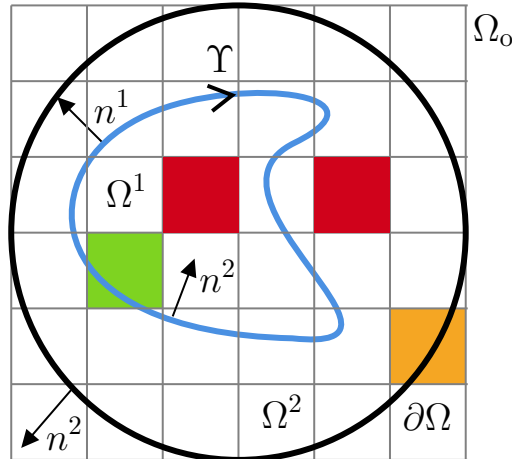


Figure 1: Schematic representation of the geometry and its discretization. Computational domain Ω_o partitioned into 6×6 square elements. The external physical boundary $\partial\Omega$ and the interface Υ not aligned with the mesh skeleton. Standard HDG elements in red, immersed boundary element (cut by $\partial\Omega$) in orange, interface element (cut by Υ) in green.

As usual in HDG, equal-order polynomial approximations are used for velocity, pressure and the mixed variable. Of course, these approximations only exist for those elements occupied (totally or partially) by fluid, that is, for those Ω_e such that $\Omega_e \cap \Omega^i \neq \emptyset$, for at least one fluid i . In addition, for the interface elements these approximations are duplicated to determine velocity, pressure and the mixed variable in each fluid. Similarly, the hybrid variable, the trace of the velocity, $\hat{\mathbf{u}}$, whose polynomial order is chosen accordingly to the highest one in the neighboring elements, is defined only on the faces (totally or partially) in the fluid, that is, when $\Gamma_f \cap \Omega^i \neq \emptyset$, for at least one fluid i . Analogously, the unknowns are duplicated for those faces intersected by the interface Υ . Figure 2 displays a schematic representation of these approximations for the three element types under analysis.

Henceforth, consider rectangular computational domains Ω_o , partitioned in rectangular-shaped elements Ω_e . In this specific context, for the element-based unknowns, Lagrange basis functions are employed as common in the case of fitted HDG methods. For the face-based unknowns, two possible bases are compared: the Lagrange basis, \mathcal{P}_{La}^k , and the Legendre basis, \mathcal{P}_{Le}^k . In Section 5.1, a comparative analysis of both bases shows the superior performance of Legendre face-based unknowns in terms of mitigating the conditioning of the global problem.

3.1 HDG local problems

Consistently with the three element types identified (standard, immersed and interface), three types of local problems must be solved. In the first case, the strong form of the local problem for *standard HDG elements* is already detailed in equation (4a), supplemented, as

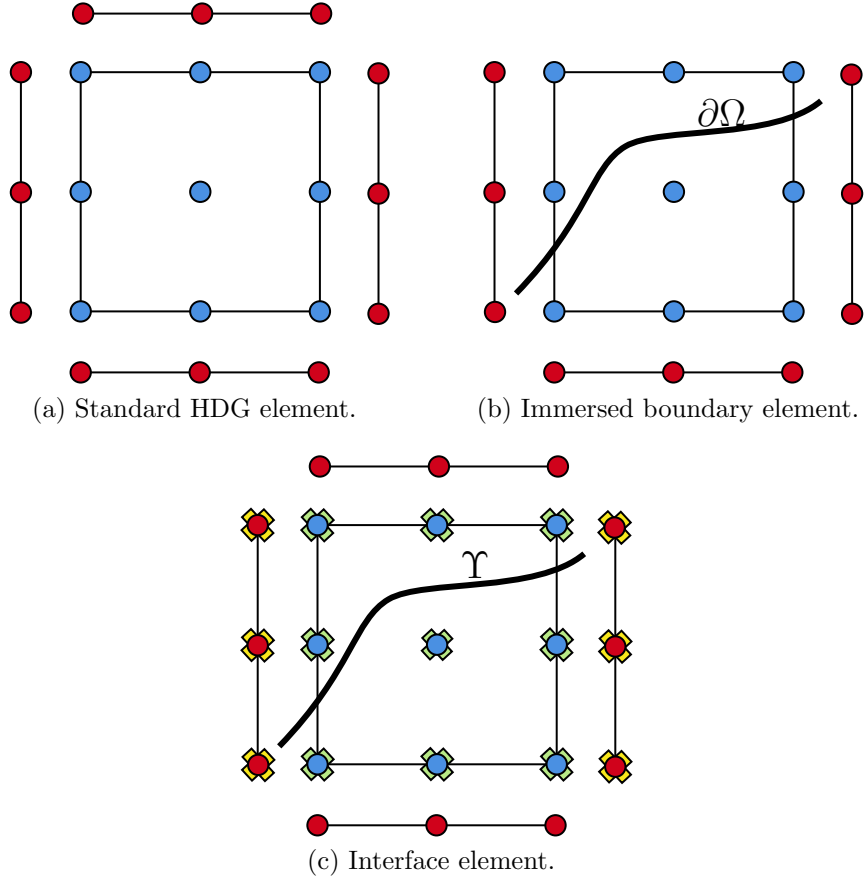


Figure 2: Schematic representation of the unknowns for the different element types. (a) Standard HDG element. (b) Immersed boundary element. (c) Interface element. Blue bullets represent local unknowns, red bullets hybrid unknowns, green crosses the doubled local unknowns employed in interface elements, and yellow crosses the doubled hybrid unknowns employed in interface cut faces.

noted earlier, with the hybrid velocity $\hat{\mathbf{u}}^i$ along $\Gamma \cap \Omega^i$ (see [60] for more details). Recall that the numerical trace of the diffusive flux must be defined. Following [47, 60] it is prescribed as

$$\widehat{(\sqrt{\mu^i} \mathbf{L}_e^i + p_e^i \mathbf{I}_{\text{n sd}})} \mathbf{n}_e := (\sqrt{\mu^i} \mathbf{L}_e^i + p_e^i \mathbf{I}_{\text{n sd}}) \mathbf{n}_e + \begin{cases} \tau(\mathbf{u}_e^i - \mathbf{u}_D), & \text{on } \hat{\Gamma}_D \cap \partial\Omega_e^i, \\ \tau(\mathbf{u}_e^i - \hat{\mathbf{u}}^i), & \text{on } \Gamma \cap \partial\Omega_e^i, \end{cases} \quad (6)$$

where τ is the stabilization parameter. Consistently with [62], this parameter is defined as $\tau := C\mu/\ell$ where $\mu := \max(\mu^1, \mu^2)$, ℓ is a characteristic length of the domain, and C is a scaling factor related to the element type, which is henceforth set equal to 3. See [62] for more details.

3.1.1 Immersed boundary elements

In what follows, $(\cdot, \cdot)_S$ and $\langle \cdot, \cdot \rangle_S$ denote the \mathcal{L}^2 -product in a generic subset $S \subset \Omega$ of dimension \mathbf{n}_{sd} and $\mathbf{n}_{\text{sd}}-1$, respectively. For immersed boundary elements, a Nitsche's penalty term [63, 64] is used to weakly impose the Dirichlet boundary conditions when $\hat{\Gamma}_D$ cuts Ω_e , namely, the weak formulation of (4a) is as follows: for all $e = 1, \dots, \mathbf{n}_{e1}$ such that $\Omega_e \cap \Upsilon = \emptyset$ and $\Omega_e \cap \partial\Omega \neq \emptyset$, given \mathbf{u}_D on Γ_D^i , \mathbf{t} on Γ_N^i , and $\hat{\mathbf{u}}^i$ on $\Gamma \cap \partial\Omega_e^i$, find $(\mathbf{L}_e^i, \mathbf{u}_e^i, p_e^i) \in [\mathcal{H}(\text{div}; \Omega_e^i)]^{\mathbf{n}_{\text{sd}} \times \mathbf{n}_{\text{sd}}} \times [\mathcal{H}^1(\Omega_e^i)]^{\mathbf{n}_{\text{sd}}} \times \mathcal{H}^1(\Omega_e^i)$ that satisfy

$$\left\{ \begin{array}{l} -(\mathbf{G}, \mathbf{L}_e^i)_{\Omega_e^i} + (\nabla \cdot (\sqrt{\mu^i} \mathbf{G}), \mathbf{u}_e^i)_{\Omega_e^i} - \langle \mathbf{G} \mathbf{n}_e, \sqrt{\mu^i} \mathbf{u}_e^i \rangle_{\Gamma_N^i \cap \overline{\Omega_e}} \\ \quad = \langle \mathbf{G} \mathbf{n}_e, \sqrt{\mu^i} \mathbf{u}_D \rangle_{\Gamma_D^i \cap \overline{\Omega_e}} + \langle \mathbf{G} \mathbf{n}_e, \sqrt{\mu^i} \hat{\mathbf{u}}^i \rangle_{\partial\Omega_e^i \setminus (\Gamma_D^i \cup \Gamma_N^i)}, \\ (\mathbf{w}, \nabla \cdot (\sqrt{\mu^i} \mathbf{L}_e^i))_{\Omega_e^i} + (\mathbf{w}, \nabla p_e^i)_{\Omega_e^i} \\ \quad - \langle \mathbf{w}, (\sqrt{\mu^i} \mathbf{L}_e^i + p_e^i \mathbf{I}_{\mathbf{n}_{\text{sd}}}) \mathbf{n}_e \rangle_{\Gamma_N^i \cap \overline{\Omega_e}} + \langle \mathbf{w}, \tau \mathbf{u}_e^i \rangle_{\partial\Omega_e^i \setminus \Gamma_N^i} + \eta h_e^{-1} \langle \mathbf{w}, \mathbf{u}_e^i \rangle_{\Gamma_D^i \cap \Omega_e} \\ \quad = (\mathbf{w}, \mathbf{s})_{\Omega_e^i} + \langle \mathbf{w}, \mathbf{t} \rangle_{\Gamma_N^i \cap \overline{\Omega_e}} + \langle \mathbf{w}, \tau \mathbf{u}_D \rangle_{\partial\Omega_e^i \cap \Gamma_D^i} \\ \quad \quad + \eta h_e^{-1} \langle \mathbf{w}, \mathbf{u}_D \rangle_{\Gamma_D^i \cap \Omega_e} + \langle \mathbf{w}, \tau \hat{\mathbf{u}} \rangle_{\partial\Omega_e^i \setminus (\Gamma_D^i \cup \Gamma_N^i)}, \\ (\nabla q, \mathbf{u}_e^i)_{\Omega_e^i} - \langle q, \mathbf{u}_e^i \cdot \mathbf{n}_e \rangle_{\Gamma_N^i \cap \overline{\Omega_e}} = \langle q, \mathbf{u}_D \cdot \mathbf{n}_e \rangle_{\Gamma_D^i \cap \overline{\Omega_e}} + \langle q, \hat{\mathbf{u}}^i \cdot \mathbf{n}_e \rangle_{\partial\Omega_e^i \setminus (\Gamma_D^i \cup \Gamma_N^i)}, \end{array} \right. \quad (7)$$

for all $(\mathbf{G}, \mathbf{w}, q) \in [\mathcal{H}(\text{div}; \Omega_e^i)]^{\mathbf{n}_{\text{sd}} \times \mathbf{n}_{\text{sd}}} \times [\mathcal{H}^1(\Omega_e^i)]^{\mathbf{n}_{\text{sd}}} \times \mathcal{H}^1(\Omega_e^i)$, where i is either 1 or 2, and where the definition in (6) of the numerical trace of the diffusive flux has been used. Recall that Nitsche's consistent penalty constant, η , must be large enough. In all the problems presented in Section 5, $\eta=10$ proved to be sufficient, and, as expected, results are insensitive to the choice of η .

Note that for those elements with pure Dirichlet boundary conditions, that is, when $\overline{\Omega_e} \cap \Gamma_N^i = \emptyset$, the problem is closed by adding the pressure condition,

$$\frac{1}{|\Omega_e^i|} (1, p_e^i)_{\Omega_e^i} = \rho_e,$$

with ρ_e an independent global variable representing the mean value of the pressure in Ω_e^i .

3.1.2 Interface elements

For the interface elements, occupied by both immiscible fluids and such that $\Omega_e \cap \partial\Omega = \emptyset$, the interface conditions couple the local variables of Ω_e^1 and Ω_e^2 (velocity, pressure and the mixed variable). Actually, at those interfaces, the average and jump operators determine the identity

$$\sum_{i=1}^2 \langle \mathbf{w}^i, \mathbf{G}^i \mathbf{n}^i \rangle_{\Upsilon} = \langle \llbracket \mathbf{w} \otimes \mathbf{n} \rrbracket, \{\mathbf{G}\} \rangle_{\Upsilon} + \langle \{\mathbf{w}\}, \llbracket \mathbf{G} \mathbf{n} \rrbracket \rangle_{\Upsilon}, \quad (8)$$

see [64]. Recall that the *jump* operator was already defined in (3) whereas the *mean*, $\{\odot\}$, is given by

$$\{\odot\} := (\odot|_{\Omega^1} + \odot|_{\Omega^2})/2, \quad (9)$$

see for instance [19]. Both follow the definition proposed in [59].

The interface elements present weak local problems as follows: for all $e = 1, \dots, \mathbf{n}_{e1}$ such that $\Omega_e \cap \Upsilon \neq \emptyset$ and $\Omega_e \cap \partial\Omega = \emptyset$, given \mathbf{u}_D on $\hat{\Gamma}_D$, \mathbf{t} on $\hat{\Gamma}_N$, $\hat{\mathbf{u}}^1$ on $\Gamma \cap \partial\Omega_e^1$, and $\hat{\mathbf{u}}^2$ on $\Gamma \cap \partial\Omega_e^2$ (i.e., $\hat{\mathbf{u}}$ on $\Gamma \cap \partial\Omega_e$), find $(\mathbf{L}_e, \mathbf{u}_e, p_e) \in [\mathcal{H}(\text{div}; \Omega_e \cap \hat{\Omega})]^{\text{nsd} \times \text{nsd}} \times [\mathcal{H}^1(\Omega_e \cap \hat{\Omega})]^{\text{nsd}} \times \mathcal{H}^1(\Omega_e \cap \hat{\Omega})$ that satisfy

$$\left\{ \begin{array}{l} -(\mathbf{G}, \mathbf{L}_e)_{\Omega_e} \\ \quad + (\nabla \cdot (\sqrt{\mu} \mathbf{G}), \mathbf{u}_e)_{\Omega_e} - \langle \mathbf{G} \mathbf{n}_e, \sqrt{\mu} \mathbf{u}_e \rangle_{\partial\Omega_e \cap \hat{\Gamma}_N} - \langle \llbracket \sqrt{\mu} \mathbf{G} \mathbf{n}_e \rrbracket, \{\mathbf{u}_e\} \rangle_{\Upsilon \cap \Omega_e} \\ \quad \quad \quad = \langle \mathbf{G} \mathbf{n}_e, \sqrt{\mu} \mathbf{u}_D \rangle_{\partial\Omega_e \cap \hat{\Gamma}_D} + \langle \mathbf{G} \mathbf{n}_e, \sqrt{\mu} \hat{\mathbf{u}} \rangle_{\partial\Omega_e \setminus (\hat{\Gamma}_D \cup \hat{\Gamma}_N)}, \\ \\ \langle \mathbf{w}, \tau \mathbf{u}_e \rangle_{\partial\Omega_e \setminus \hat{\Gamma}_N} \\ \quad + (\mathbf{w}, \nabla \cdot (\sqrt{\mu} \mathbf{L}_e))_{\Omega_e} - \langle \mathbf{w}, \sqrt{\mu} \mathbf{L}_e \mathbf{n}_e \rangle_{\partial\Omega_e \cap \hat{\Gamma}_N} - \langle \{\mathbf{w}\}, \llbracket \sqrt{\mu} \mathbf{L}_e \mathbf{n}_e \rrbracket \rangle_{\Upsilon \cap \Omega_e} \\ \quad + (\mathbf{w}, \nabla p_e)_{\Omega_e} - \langle \mathbf{w}, p_e \mathbf{n}_e \rangle_{\partial\Omega_e \cap \hat{\Gamma}_N} - \langle \{\mathbf{w}\}, \llbracket p_e \mathbf{n}_e \rrbracket \rangle_{\Upsilon \cap \Omega_e} \\ \quad \quad \quad = (\mathbf{w}, \mathbf{s})_{\Omega_e} + \langle \mathbf{w}, \mathbf{t} \rangle_{\partial\Omega_e \cap \hat{\Gamma}_N} + \langle \mathbf{w}, \tau \mathbf{u}_D \rangle_{\partial\Omega_e \cap \hat{\Gamma}_D} \\ \quad \quad \quad \quad + \langle \mathbf{w}, \tau \hat{\mathbf{u}} \rangle_{\partial\Omega_e \setminus (\hat{\Gamma}_D \cup \hat{\Gamma}_N)} + \langle \{\mathbf{w}\}, \gamma(\nabla \cdot \mathbf{n}_e^1) \mathbf{n}_e^1 \rangle_{\Upsilon \cap \Omega_e}, \\ \\ (\nabla q, \mathbf{u}_e)_{\Omega_e} - \langle q, \mathbf{u}_e \cdot \mathbf{n}_e \rangle_{\partial\Omega_e \cap \hat{\Gamma}_N} - \langle \llbracket q \mathbf{n}_e \rrbracket, \{\mathbf{u}_e\} \rangle_{\Upsilon \cap \Omega_e} \\ \quad \quad \quad = \langle q, \mathbf{u}_D \cdot \mathbf{n}_e \rangle_{\partial\Omega_e \cap \hat{\Gamma}_D} + \langle q, \hat{\mathbf{u}} \cdot \mathbf{n}_e \rangle_{\partial\Omega_e \setminus (\hat{\Gamma}_D \cup \hat{\Gamma}_N)}, \end{array} \right. \quad (10)$$

for all $(\mathbf{G}, \mathbf{w}, q) \in [\mathcal{H}(\text{div}; \Omega_e \cap \hat{\Omega})]^{\text{nsd} \times \text{nsd}} \times [\mathcal{H}^1(\Omega_e \cap \hat{\Omega})]^{\text{nsd}} \times \mathcal{H}^1(\Omega_e \cap \hat{\Omega})$, where the numerical trace of the diffusive flux defined in (6) has been used and the interface conditions (4b) have been imposed such that symmetry is preserved. Actually, it is worth noticing that (10) preserves the symmetry of the Stokes problem. Moreover, as shown in the numerical examples, since in each element $|\partial\Omega_e \setminus \hat{\Gamma}_N| > |\Upsilon|$, there is no need for adding any extra stabilization term along Υ . Note also that the following three particularizations of (8) have been exploited:

$$\begin{aligned} \sum_{i=1}^2 \langle \mathbf{G} \mathbf{n}^i, \sqrt{\mu^i} \mathbf{u}^i \rangle_{\Upsilon} &= \langle \llbracket \mathbf{u} \otimes \mathbf{n} \rrbracket, \{\sqrt{\mu} \mathbf{G}\} \rangle_{\Upsilon} + \langle \{\mathbf{u}\}, \llbracket \sqrt{\mu} \mathbf{G} \mathbf{n} \rrbracket \rangle_{\Upsilon}, \\ \sum_{i=1}^2 \langle \mathbf{w}^i, (\sqrt{\mu^i} \mathbf{L}^i + p^i \mathbf{I}_{\text{nsd}}) \mathbf{n}^i \rangle_{\Upsilon} &= \langle \llbracket \mathbf{w} \otimes \mathbf{n} \rrbracket, \{\sqrt{\mu} \mathbf{L} + p \mathbf{I}_{\text{nsd}}\} \rangle_{\Upsilon} + \langle \{\mathbf{w}\}, \llbracket (\sqrt{\mu} \mathbf{L} + p \mathbf{I}_{\text{nsd}}) \mathbf{n} \rrbracket \rangle_{\Upsilon}, \\ \sum_{i=1}^2 \langle q^i, \mathbf{u}^i \cdot \mathbf{n}^i \rangle_{\Upsilon} &= \langle \llbracket q \mathbf{n} \rrbracket, \{\mathbf{u}\} \rangle_{\Upsilon} + \langle \{q\}, \llbracket \mathbf{u} \cdot \mathbf{n} \rrbracket \rangle_{\Upsilon}. \end{aligned}$$

Finally, as before, when $\partial\Omega_e \cap \hat{\Gamma}_N = \emptyset$, the problem is closed by adding the pressure condition,

$$\frac{1}{|\Omega_e|} \sum_{i=1}^2 (p_e^i, 1)_{\Omega_e \cap \Omega^i} = \rho_e.$$

3.2 HDG global problem

The previous section details element-by-element problems that allow to express the local variables $(\mathbf{L}_e^i, \mathbf{u}_e^i, p_e^i)$ in terms of the global unknowns $(\hat{\mathbf{u}}^i, \rho_e)$. The global problem represented by the *transmission conditions* (4c) solves for the global unknowns $(\hat{\mathbf{u}}^i, \rho_e)$. By definition, $\hat{\mathbf{u}}^i$ is uniquely defined on each face of $\Gamma \cap \Omega^i$ thus condition $[[\mathbf{u}^i \otimes \mathbf{n}^i]] = \mathbf{0}$ is automatically satisfied because of (5).

The integral formulation resulting from the transmission condition is as follows: given \mathbf{u}_D on $\hat{\Gamma}_D$, \mathbf{t} on $\hat{\Gamma}_N$, and the expressions of the local variables $(\mathbf{L}_e^i, \mathbf{u}_e^i, p_e^i)$ in terms of the global unknowns $(\hat{\mathbf{u}}^i, \rho_e)$ from the local problems, find $(\hat{\mathbf{u}}^i, \rho_e) \in [\mathcal{H}^{\frac{1}{2}}(\Gamma \cap \partial\Omega_e^i)]^{\text{nsd}} \times \mathbb{R}$ that satisfy

$$\sum_{e=1}^{\mathbf{n}_{e1}} \sum_{i=1}^2 \left\{ \langle \hat{\mathbf{w}}, (\sqrt{\mu^i} \mathbf{L}_e^i + p_e^i \mathbf{I}_{\text{nsd}}) \mathbf{n}_e \rangle_{\partial\Omega_e^i \setminus (\hat{\Gamma}_D \cup \hat{\Gamma}_N)} + \langle \hat{\mathbf{w}}, \tau \mathbf{u}_e^i \rangle_{\partial\Omega_e^i \setminus (\hat{\Gamma}_D \cup \hat{\Gamma}_N)} - \langle \hat{\mathbf{w}}, \tau \hat{\mathbf{u}}^i \rangle_{\partial\Omega_e^i \setminus (\hat{\Gamma}_D \cup \hat{\Gamma}_N)} \right\} = 0, \quad (11a)$$

for all $\hat{\mathbf{w}} \in [\mathcal{L}_2(\Gamma \cap \partial\Omega_e^i)]^{\text{nsd}}$. In addition to the transmission conditions, for all elements not affected by the Neumann boundary condition, that is, for $e = 1, \dots, \mathbf{n}_{e1}$ such that $\overline{\Omega_e} \cap \hat{\Gamma}_N = \emptyset$, the following compatibility condition is considered

$$\sum_{i=1}^2 \left\{ \langle \hat{\mathbf{u}}^i \cdot \mathbf{n}_e, 1 \rangle_{\partial\Omega_e^i \setminus \hat{\Gamma}_D} + \langle \mathbf{u}_D \cdot \mathbf{n}_e, 1 \rangle_{\partial\Omega_e^i \cap \hat{\Gamma}_D} \right\} = 0. \quad (11b)$$

The above equation is derived from the divergence-free condition, where the continuity of velocity along the interface Υ , see (4b), has been exploited.

Note that the global problem described by (11) is not directly affected by the interface because its influence is taken into account in the local problems by the terms along Υ . Also, recall that the additional pressure condition, presented in Remark 3, is required when $\hat{\Gamma}_N = \emptyset$.

3.3 HDG postprocess and degree adaptivity

Following [60, 65–68], for $i = 1, 2$, the discrete functional space composed of polynomial functions of degree at most $k+1$ is defined as

$$\mathcal{V}_\star^h(\hat{\Omega}) := \{v \in \mathcal{L}_2(\hat{\Omega}) \mid v|_{\Omega_e^i} \in \mathcal{P}^{k+1}(\Omega_e^i), \forall e = 1, \dots, \mathbf{n}_{e1}, \text{ and } \forall i = 1, 2\}. \quad (12)$$

Then, the accuracy of the velocity field approximation can be enhanced, achieving convergence of order $k+2$, by solving an additional, computationally efficient element-by-element problem. For $e = 1, \dots, \mathbf{n}_{e1}$, find the superconvergent velocity field $\mathbf{u}_\star \in [\mathcal{V}_\star^h(\hat{\Omega})]^{\text{nsd}}$ such that $\mathbf{u}_{\star,e}^i = \mathbf{u}_\star|_{\Omega_e^i}$ for $i = 1, 2$ and

$$\begin{cases} -\nabla \cdot (\sqrt{\mu^i} \nabla \mathbf{u}_{\star,e}^i) = \nabla \cdot \mathbf{L}_e^i & \text{in } \Omega_e^i, \\ \sqrt{\mu^i} \nabla \mathbf{u}_{\star,e}^i \mathbf{n}_e = -\mathbf{L}_e^i \mathbf{n}_e & \text{on } \partial\Omega_e^i \cup (\Upsilon \cap \Omega_e), \end{cases} \quad (13)$$

and such that the mean superconvergent velocity satisfies

$$(\mathbf{u}_{\star,e}^i, 1)_{\Omega_e^i} = (\mathbf{u}_e^i, 1)_{\Omega_e^i}. \quad (14)$$

Hence, the weak problems for each fluid are: for $e = 1, \dots, \mathbf{n}_{e1}$ and $i = 1, 2$, solve

$$\begin{aligned} (\nabla \mathbf{w}_\star^i, \sqrt{\mu^i} \nabla \mathbf{u}_{\star,e}^i)_{\Omega_e^i} &= -(\nabla \mathbf{w}_\star^i, \mathbf{L}_e^i)_{\Omega_e^i}, \\ (\mathbf{u}_{\star,e}^i, 1)_{\Omega_e^i} &= (\mathbf{u}_e^i, 1)_{\Omega_e^i}, \end{aligned} \quad (15)$$

with \mathbf{w}_\star^i being a test function of polynomial degree at most $k+1$ in Ω_e^i .

Consistently with [49], the following element-wise measure of the error is employed

$$E_e := \max_{i=1,2} \left\{ (\mathbf{u}_{\star,e}^i - \mathbf{u}_e^i, \mathbf{u}_{\star,e}^i - \mathbf{u}_e^i)_{\Omega_e^i}^{1/2} / (\mathbf{u}_{\star,e}^i, \mathbf{u}_{\star,e}^i)_{\Omega_e^i}^{1/2} \right\}, \quad \text{for } e = 1, \dots, \mathbf{n}_{e1}. \quad (16)$$

Obviously, for values of $(\mathbf{u}_{\star,e}^i, \mathbf{u}_{\star,e}^i)_{\Omega_e^i}^{1/2}$ below a prescribed tolerance the absolute error is employed.

The strategy depicted in [49] allows to attain the desired accuracy ε on the error E_e by locally adapting the degree of the HDG approximation. Problem (2) is thus solved iteratively increasing or decreasing, for each element Ω_e , the local degree k_e of approximation as

$$\delta k_e = \left\lceil \frac{\log(\varepsilon/E_e)}{\log(h_e)} \right\rceil, \quad (17)$$

with $\lceil \cdot \rceil$ being the ceiling function and h_e the local mesh size of element Ω_e . The procedure ends when $\delta k_e = 0$, for $e = 1, \dots, \mathbf{n}_{e1}$.

4 Computational setting for non-conforming meshes

In this section, technical details related to the treatment of the unfitted interface, the numerical quadrature in the presence of NURBS and the element extension strategy to ensure robustness with respect to badly cut cells are presented.

4.1 Identification of the two fluid subdomains

Given the unfitted NURBS interface, see (1), the two fluid subdomains Ω^i , $i = 1, 2$ need to be characterized. Without loss of generality, only the interface Υ splitting domains Ω^1 and Ω^2 is considered (i.e., assume that the external boundary $\partial\Omega$ is aligned with the mesh boundary $\partial\Omega_o$). Moreover, the interface Υ is assumed closed, orientable, and not touching the boundary $\partial\Omega$. Hence, the interior subdomain is denoted by Ω^1 whereas the exterior one is described as Ω^2 . A schematic representation of the setup is reported in Figure 3.

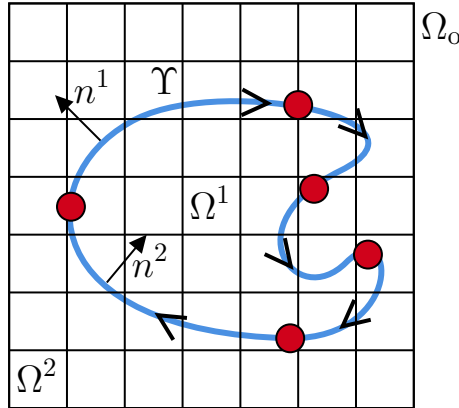


Figure 3: Schematic representation of an unfitted NURBS interface Υ in the computational domain Ω_o .

The interface Υ is clockwise oriented and is composed of 5 NURBS curves separated by red bullets. The outward unit normal to Ω^i is denoted by \mathbf{n}^i , for $i = 1, 2$.

To identify the two fluid domains, this work follows the procedure presented in [32]. The idea is to decompose the problem element-wise by identifying, for each element, the regions Ω_e^i for $i = 1, 2$ and then obtain each fluid domain as $\Omega^i = \bigcup_{e=1}^{ne1} \Omega_e^i$.

First, the elements cut by the NURBS are identified and the intersection points between the internal skeleton Γ and Υ are located and ordered according to the orientation of Υ (see Appendix A for the details of this step). Consequently, Υ_e is defined as the portion of Υ inside element Ω_e , i.e., $\Upsilon_e := \Upsilon \cap \Omega_e$. Note that, by definition, Υ_e is a continuous curve and it can be composed of several NURBS curves, that is,

$$\Upsilon_e = \bigcup_{j \in \mathcal{J}_e} \Upsilon_e^j \quad \text{with } \Upsilon_e^j := \mathbf{C}_{\Upsilon}^j([\lambda_{e,1}^j, \lambda_{e,2}^j]), \quad (18)$$

where \mathcal{J}_e is the set of coefficients j of the NURBS curves \mathbf{C}_{Υ}^j inside Ω_e , while $\lambda_{e,1}^j$ and $\lambda_{e,2}^j$ are the extrema of \mathbf{C}_{Υ}^j in Ω_e .

For each cut element Ω_e (see, e.g., the green element in Figure 1), the two regions, Ω_e^1 and Ω_e^2 , are constructed connecting the mesh vertices and the ordered intersection points. Starting from the first intersection point between Γ and Υ_e and travelling along Υ_e towards the left or towards the right, two sides of Υ_e are identified. Depending on the orientation of Υ_e , the fluid index i of each adjacent region is determined: when Υ_e is clockwise oriented, the right region is Ω_e^1 , whereas the left one is denoted by Ω_e^2 , and vice versa when Υ_e is counter-clockwise oriented. This procedure is sketched in Figure 4a and it can also be generalized to the case of unfitted boundary $\partial\Omega$.

The assignment of the appropriate fluid index to the remaining, uncut elements is performed iteratively. Starting from a neighboring element, with a common face, for which such information has already been determined, the fluid index of the uncut element is

inherited across the shared face.

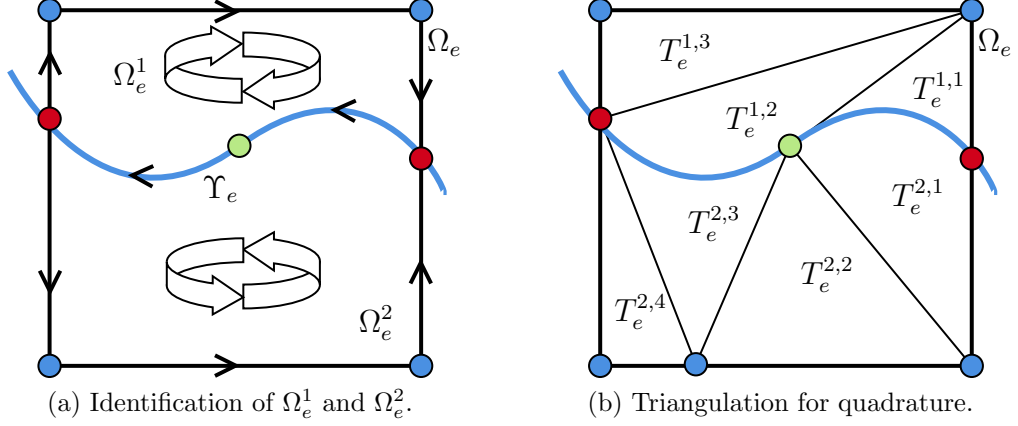


Figure 4: Element Ω_e cut in two regions by an interface Υ_e . (a) Identification of Ω_e^1 and Ω_e^2 . (b) Triangulation for quadrature. The interface is composed of two NURBS curves connected at the green bullet. The red bullets denote the intersections between Υ and $\partial\Omega_e$ and the blue ones are the vertices of Ω_e and of the triangulation for quadrature.

4.2 Quadrature in elements and faces cut by NURBS

Specific numerical techniques are used to integrate along cut faces (i.e., along NURBS curves) and in cut elements, whereas uncut faces and uncut elements employ standard HDG quadratures.

Quadratures along cut faces only require the proper mapping between each segment of the face and the reference domain of the chosen quadrature. Typically Gauss-Legendre quadratures are used along each segment.

The quadrature along NURBS curves is treated element-wise. For a generic scalar function f , the quadrature along the portion of NURBS interface Υ_e is defined as

$$\int_{\Upsilon_e} f \, dl = \sum_{j \in \mathcal{J}_e} \int_{\lambda_1^j}^{\lambda_2^j} f(\mathbf{C}_{\Upsilon}^j(\lambda)) \|J_{\mathbf{C}_{\Upsilon}^j}(\lambda)\| \, d\lambda,$$

where $\|J_{\mathbf{C}_{\Upsilon}^j}\|$ is the norm of the differential of the parametrization of the NURBS curve \mathbf{C}_{Υ}^j describing Υ_e^j . The integrals are approximated using the 1D Gauss-Legendre quadrature defined in the parametric space $[\lambda_{e,1}^j, \lambda_{e,2}^j]$ and mapped along \mathbf{C}_{Υ}^j . The same procedure can be employed also for unfitted external boundaries.

The quadrature within a generic region Ω_e^i involves multiple steps. Firstly, the region Ω_e^i undergoes a partitioning process, guided by Lee's visibility algorithm [69], which is essential

to ensure the accuracy of the quadrature, as emphasized in [14]. The procedure, presented in Appendix B, constructs a triangular partition (see Figure 4b) of each subregion Ω_e^i such that

$$\Omega_e^i = \bigcup_{l=1}^{\mathbf{n}_{\Omega_e^i}} T_e^{i,l},$$

with $\mathbf{n}_{\Omega_e^i}$ the total number of triangles composing Ω_e^i . The resulting triangulation consists of two types of elements: affine and curved. The former are handled using standard isoparametric mapping in finite elements. The latter, which require a special treatment, are constructed with at most one curved edge, described by one NURBS curve.

Given a generic scalar function f , the quadrature in Ω_e^i is obtained as the sum of the quadrature in each triangle identified according to the previous procedure, that is,

$$\int_{\Omega_e^i} f(x, y) \, dx dy = \sum_{l=1}^{\mathbf{n}_{\Omega_e^i}} \int_{T_e^{i,l}} f(x, y) \, dx dy.$$

When $T_e^{i,l}$ is an affine triangle, the standard Gauss–Legendre quadrature is employed, whereas the quadrature procedure proposed in [12] for NEFEM is employed in the case of a curved element $T_e^{i,l}$. In this case, the Gauss–Legendre quadrature is constructed in the rectangle $R := [\lambda_{e,1}^j, \lambda_{e,2}^j] \times [0, 1]$ which is transformed to $T_e^{i,l}$ by means of the affine mapping

$$\boldsymbol{\psi}(\lambda, \theta) := (1 - \theta)\mathbf{C}^j(\lambda) + \theta \mathbf{x}_3, \quad \forall \lambda \in [\lambda_{e,1}^j, \lambda_{e,2}^j], \quad \forall \theta \in [0, 1],$$

with \mathbf{x}_3 being the vertex of the triangle not lying on the NURBS curve. Then, it follows that

$$\int_{T_e^{i,l}} f(x, y) \, dx dy = \int_R f(\boldsymbol{\psi}(\lambda, \theta)) |J_{\boldsymbol{\psi}}(\lambda, \theta)| \, d\lambda d\theta,$$

where $|J_{\boldsymbol{\psi}}|$ is the determinant of the Jacobian of the transformation $\boldsymbol{\psi}$.

4.3 Element extension for badly cut cells

It is well-known that unfitted methods suffer in the presence of elements, cut by the interface or the boundary, such that the portion of the computational volume is small with respect to the volume of the entire element. To measure such cuts, the parameter

$$\alpha_e^i := \frac{|\Omega_e^i|}{|\Omega_e|}, \quad e = 1, \dots, \mathbf{n}_{e1}, \quad i = 1, 2, \quad (19)$$

is defined as the ratio between the region occupied by fluid i , i.e., Ω_e^i , and the entire element Ω_e . The smallest cut in a computational domain Ω_o is denoted by $\alpha := \min_e \min_i \alpha_e^i$. An element is said to be badly cut when $\alpha_e^i < \alpha_{\min}$, with α_{\min} a user-defined value, usually set to $\alpha_{\min}=0.3$ consistently with the literature, see, e.g. [55, 56].

To address badly cut cells, the element extension method proposed in [32] is used. If $\alpha_e^i < \alpha_{\min}$ for $i = 1, 2$, the element extension strategy, depicted in Figure 5, performs the integration using the shape functions and elemental nodal distribution of a well-cut, neighboring element. More precisely, the procedure executes the following operations:

- (1) It erases the element-based unknowns of the badly cut cell.
- (2) It extends the element-based approximation (and, hence, the quadrature) from a selected neighboring element to the badly cut cell.
- (3) It erases the face-based unknowns along the face shared by the two elements.
- (4) It preserves the face-based unknowns of the badly cut cell.

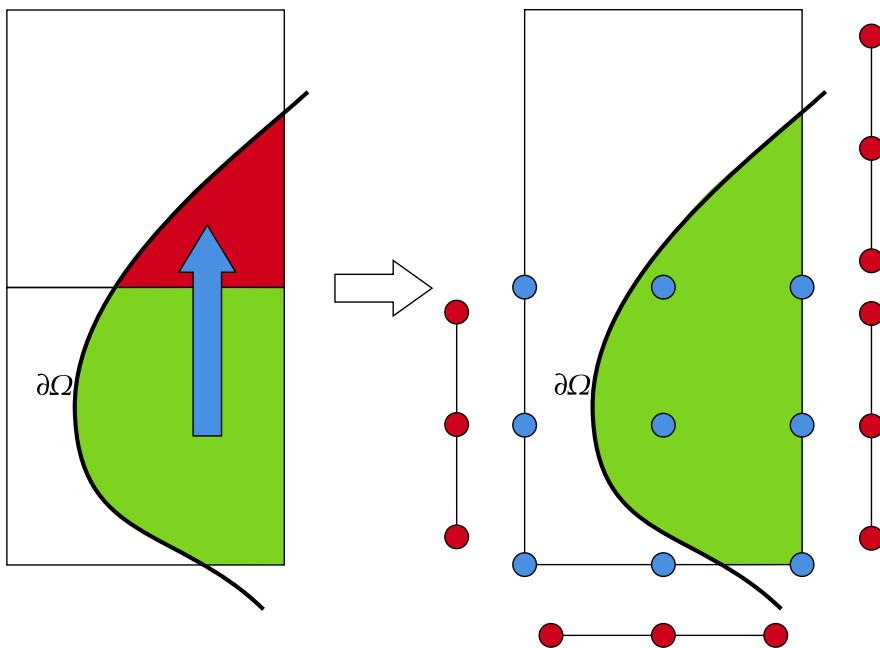


Figure 5: Element extension strategy. Left: initial configuration with badly cut cell (red) and well-cut cell (green). Right: extended element. Blue bullets are the element-based unknowns and red bullets the face-based unknowns of the resulting extended element.

For each badly cut cell, potential extensions are assessed based on three factors: (i) to maximize the combined area; (ii) to minimize the Euclidean distance between element centers; (iii) to penalize previously extended elements. The element with the highest combined score of these factors is extended onto the badly cut one. In two-fluid problems, a stronger penalty is used to discourage multiple extensions per element owing to inter-region coupling, thus minimizing the local problem size.

5 Numerical results

In this section, the unfitted HDG method with exact treatment of NURBS geometry is tested for a series of 2D problems featuring a single fluid and two immiscible fluids. After assessing the robustness of the method in the presence of badly cut faces and badly cut cells in Section 5.1, numerical experiments show the optimal convergence and high-fidelity accuracy achieved by the scheme in the case of an unfitted external boundary (Section 5.2) and an unfitted interface (Section 5.3) described by means of NURBS. Finally, the suitability of the proposed approach to simulate microfluidic systems featuring complex geometries is showcased in Sections 5.4 and 5.5 for one and two-fluid problems.

5.1 Robustness with respect to badly cut faces and cells

As noted earlier, it is well known that unfitted methods suffer from badly cut cells. However, in HDG face/skeleton unknowns and integrals play a prominent role. Here, a synthetic problem with manufactured solution is used to study the effect of badly cut faces and badly cut cells on the discretization error and on the condition number of the matrices arising from the HDG formulation.

Consider a one-fluid problem on the domain Ω , with Dirichlet boundary conditions on the unfitted boundary $\partial\Omega$. The detailed definition of the domain Ω is provided in the following subsections, whereas the computational domain is set to $\Omega_o=(0,1)^2$. Given a viscosity $\mu=1$, the Dirichlet datum \mathbf{u}_D and the source term \mathbf{s} are analytically obtained from the expressions of the Stokes velocity and pressure fields, see [70], given by

$$\mathbf{u}^{\text{ref}} = \begin{pmatrix} x^2(1-x)^2(2y-6y^2+4y^3) \\ -y^2(1-y)^2(2x-6x^2+4x^3) \end{pmatrix}, \quad p^{\text{ref}} = x(1-x). \quad (20)$$

The quantities of interest in the present study are the condition numbers κ^{loc} and κ^{glob} , computed using the Euclidean norm, of the HDG local and global matrices, respectively. Consistently with the definition of the element ratio α_e^i , see (19), for each face $\Gamma_f \subset \Gamma$, the ratio between the computational face $\Gamma_f \cap \Omega^i$ and the entire face Γ_f is defined as

$$\beta_f^i := \frac{|\Gamma_f \cap \Omega^i|}{|\Gamma_f|}, \quad f = 1, \dots, \mathbf{n}_{\text{fc}}, \quad i = 1, 2, \quad (21)$$

and $\beta := \min_f \min_i \beta_f^i$ denotes the smallest face cut in the computational domain.

5.1.1 Badly cut faces

Consider the M-shaped domain (see Figure 6), defined as $\Omega := \Omega_R \setminus \Omega_T$, with $\Omega_R=(0.25, 0.75) \times (0.25, 1)$ and Ω_T being the triangular region with vertices $(0.25, 1)$, $(0.75, 1)$ and $(0.5, 0.75 +$

ε), $\varepsilon > 0$. The computational domain is the square $\Omega_o = (0, 1)^2$, composed of a 4×4 mesh of square elements.

By construction, all the elements and faces of the M-shaped domain are well-cut, except for the vertical face of extrema $(0.5, 0.75)$ and $(0.5, 0.75 + \varepsilon)$. The influence on the global condition number of the decreasing length of this face is studied for $\varepsilon \in \{5 \times 10^{-3}, 5 \times 10^{-2}, 10^{-1}, 1.5 \times 10^{-1}\}$, leading to $\beta \in \{2\%, 20\%, 40\%, 60\%\}$ of the entire face, while always maintaining well-cut elements with $\alpha > 50\%$.

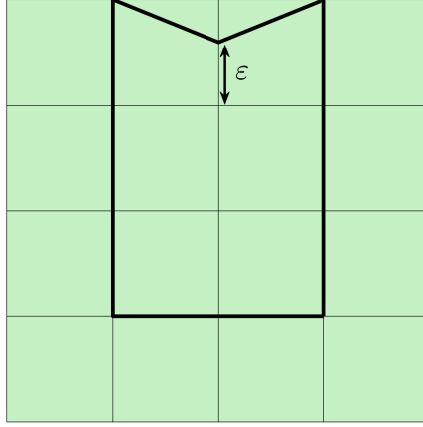


Figure 6: M-shaped domain with $\varepsilon = 1.5 \times 10^{-1}$ ($\beta = 60\%$ of the entire face).

Figure 7 shows the global condition number κ^{glob} as a function of the smallest face cut β , using nodal and modal basis functions of polynomial degree $k = 1, \dots, 4$ for the hybrid variable. More precisely, Lagrange basis functions $\mathcal{P}_{\text{La}}^k$ are compared with Legendre basis functions $\mathcal{P}_{\text{Le}}^k$. For the element-based unknowns, 2D Lagrange tensor basis functions with Fekete nodal distribution are employed, guaranteeing the optimal condition number and accuracy for standard, uncut, elements.

The results show that, whilst modal basis functions yield a condition number κ^{glob} independent of β for any polynomial degree, nodal basis functions tend to suffer when small cut faces appear in the domain and this phenomenon becomes even more severe for high-order approximations. Note that this is consistent with the recent results on the hybrid high order method (a close relative of HDG) presented in [71]. Indeed, by construction, Lagrange basis functions are equal to zero at all nodes except for the one where they are centered. Moreover, the contribution of each basis function progressively concentrates in the vicinity of its center as the polynomial degree k increases (see Figure 7 for the Lagrange basis functions of degree 4 in the interval $[-1, 1]$). Thus, when integrating over a portion of a face, the influence of the Lagrange functions centered at nodes lying outside of the domain significantly decreases, leading to small contributions that tend to zero as the polynomial degree k increases and, consequently, to an ill-conditioning of the matrix. On the contrary, Legendre basis functions feature a larger support where each polynomial function is different than zero (see Figure 7), reducing the effect of small face

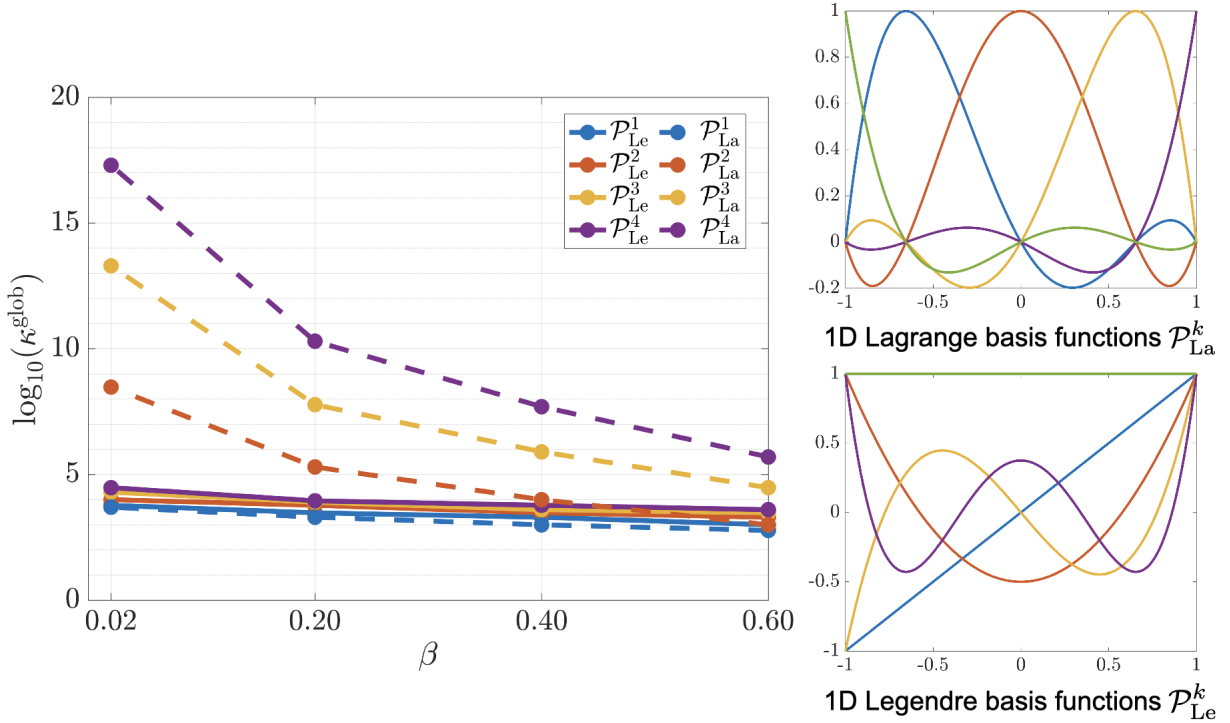


Figure 7: M-shaped domain. Comparison of the global condition number $\log_{10}(\kappa^{\text{glob}})$ as a function of the smallest face cut β using Lagrange $\mathcal{P}_{\text{La}}^k$ (dashed lines) and Legendre $\mathcal{P}_{\text{Le}}^k$ (continuous lines) basis functions of degree $k = 1, \dots, 4$ for the face-based variable.

cuts during quadrature. Thus, Legendre basis functions are employed for the face-based variables in all the numerical results presented henceforth.

5.1.2 Badly cut cells

The second test case considers the domain $\Omega := \Omega_S \setminus \bigcup_{i=1}^4 \Omega_A^i$ in Figure 8, obtained by subtracting from the square region $\Omega_S = (0.1, 0.9)^2$ the four circular arcs Ω_A^i , $i = 1, \dots, 4$ of radius 0.15 and centered in $(0.1, 0.1)$, $(0.9, 0.1)$, $(0.9, 0.9)$ and $(0.1, 0.9)$. The computational domain is the square $\Omega_o = (0, 1)^2$, partitioned in a mesh of 4×4 square elements.

In this configuration, all faces are well-cut, with $\beta > 60\%$. Nonetheless, whilst most cut elements feature a portion of occupied area equal to 60%, the four ones at the corners are badly cut, with α dropping to 6%. To address the numerical issues arising from such small cuts, the element extension strategy presented in Section 4.3 is employed, leading to the extended elements in Figure 8b.

It is worth recalling that the HDG global problem, see (11), only involves face integrals. On the contrary, HDG local problems (see Sections 3.1.1 and 3.1.2) also feature element integrals and can experience ill-conditioning issues when small elements appear in the computational mesh. Of course, since the HDG local problems are employed to construct

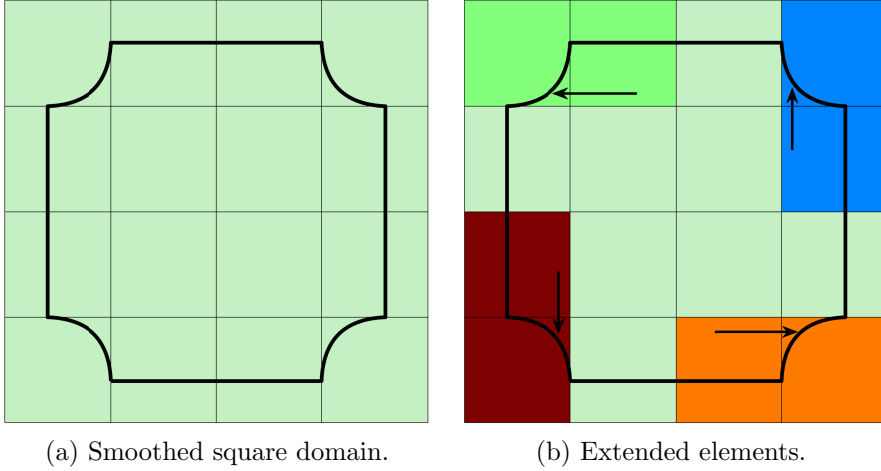


Figure 8: Smoothed square domain and extension procedure to treat badly cut cells.

the hybrid system of the HDG global problem, an indirect effect of badly cut cells on the condition number κ^{glob} is also present but this can be controlled by the element extension procedure as reported in Section 5.2. Thus, the following study focuses on the local systems only.

Figure 9 displays the condition number κ^{loc} for the HDG local problems, with and without element extensions. As expected, the badly cut cells are responsible for the local condition number to quickly deteriorate, achieving unmanageable values (Figure 9b). By means of element extension, the negative effects of badly cut cells are mitigated, reducing the local condition number of up to 5 orders of magnitude, as reported in Figure 9a. Of course, this procedure also affects the extended, previously well cut, elements, which experience a degradation of the condition number of the local problem: for instance, an extrapolation over 6% of the element area yields an increase of κ^{loc} of about 2 orders of magnitude compared to its initial value. Nonetheless, as it will be detailed in Section 5.2, the condition number of the HDG global problem remains bounded even when element extension is performed, thus guaranteeing the robustness of the method and the accuracy of the global solution.

Similarly, the element-by-element map of the velocity error, measured in the $\mathcal{L}^2(\Omega_e)$ norm, is presented in Figure 10. The results confirm the conclusions from Figure 9, confirming the capability of element extension to significantly reduce the error of the local variable in badly cut cells, while slightly worsening the approximation in the extended region.

The above results are obtained with a discretization employing Lagrange polynomial functions of degree 4 for the element-based unknowns and a Legendre basis of degree 4 for the face-based variable. Alternative solutions, not reported here for brevity, were explored for the treatment of the element-based unknowns but no significant gain in accuracy nor

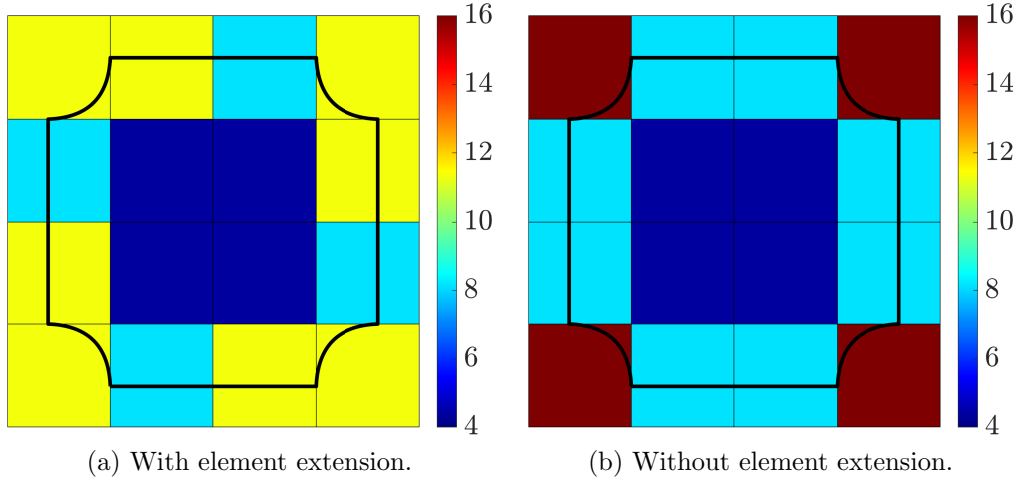


Figure 9: Smoothed square domain. Element-by-element condition number $\log_{10}(\kappa^{\text{loc}})$ of the HDG local problem (a) with and (b) without element extension.

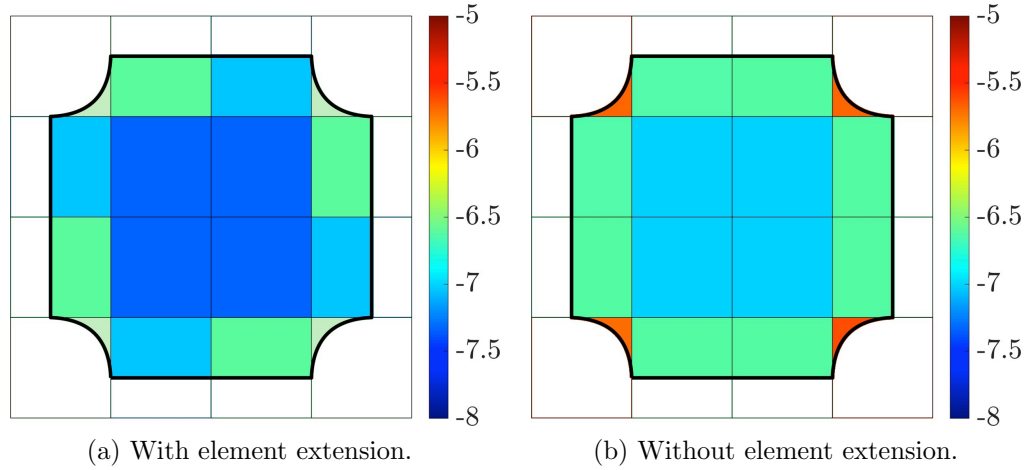


Figure 10: Smoothed square domain. Element-by-element map of the error $\|\mathbf{u} - \mathbf{u}^{\text{ref}}\|_{\mathcal{L}^2(\Omega_e)}$ (a) with and (b) without element extension.

robustness was observed. Thus, Lagrange basis functions with Fekete nodes are henceforth employed to approximate the element-based variables in the following simulations.

5.2 Taylor-Couette flow with unfitted boundary

A two-dimensional, one-fluid, coaxial Taylor-Couette flow is considered to numerically assess the accuracy and optimal convergence property of the unfitted HDG method, in the presence of an exact boundary represented via NURBS. The domain Ω consists of

two coaxial circles of radii $R_{\text{int}}=1/6$ and $R_{\text{ext}}=1/3$, centered in $(0.5, 0.5)$, and rotating with angular velocities $\omega_{\text{int}}=0$ and $\omega_{\text{ext}}=1$, respectively. Setting $\mu=1$, the Taylor-Couette velocity and pressure fields are defined as

$$\mathbf{u}^{\text{ref}} = \begin{pmatrix} -Ay - By/(x^2 + y^2) \\ Ax + Bx/(x^2 + y^2) \end{pmatrix}, \quad p^{\text{ref}} = 1, \quad (22)$$

with

$$A := \frac{\omega_{\text{ext}}R_{\text{ext}}^2 - \omega_{\text{int}}R_{\text{int}}^2}{R_{\text{ext}}^2 - R_{\text{int}}^2}, \quad B := \frac{(\omega_{\text{int}}\omega_{\text{ext}})R_{\text{ext}}^2R_{\text{int}}^2}{R_{\text{ext}}^2 - R_{\text{int}}^2},$$

and verify the one-fluid Stokes equations with zero body forces and Dirichlet conditions \mathbf{u}_D (obtained from the analytical velocity \mathbf{u}^{ref}) on the entire boundary $\partial\Omega$, see, e.g., [62].

The domain Ω is immersed in a computational domain $\Omega_o=(0, 1)^2$, featuring a Cartesian mesh of square elements. A detail of the 8×8 mesh, in the region $(0.125, 0.875)^2$, is displayed in Figure 11a, along with an example of element extension (Figure 11b). The module of the velocity field computed on the same mesh using polynomial approximation of degree 4 is reported in Figure 11c.

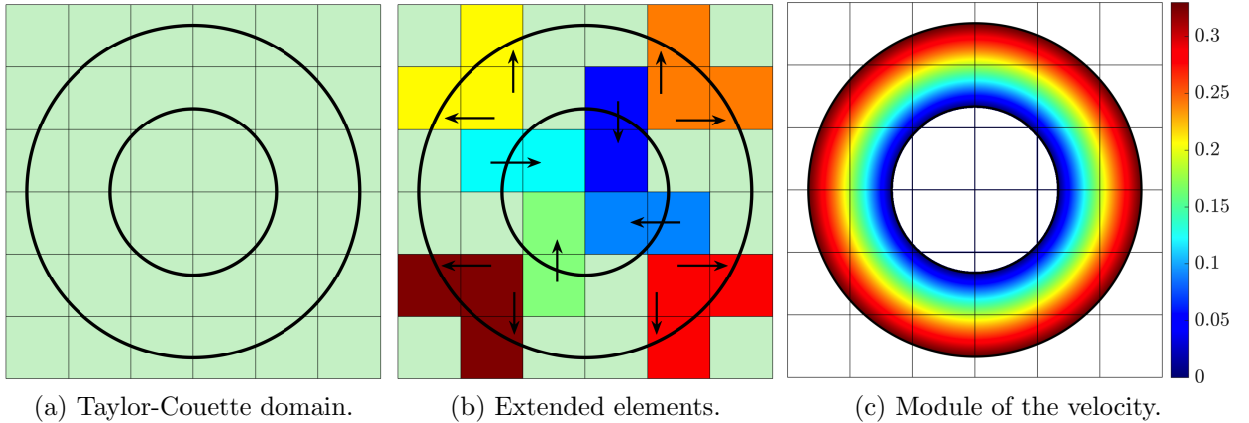


Figure 11: Taylor-Couette domain. (a) Detail of the computational domain in the region $(0.125, 0.875)^2$. (b) Element extension to avoid badly cut cells. (c) Module of the velocity approximated using polynomial functions of degree $k = 4$.

A mesh convergence study is then performed using a set of Cartesian structured meshes composed of 2×2 , 4×4 , 8×8 , 16×16 , and 32×32 square elements, for polynomial degree approximations ranging from $k = 1$ up to $k = 4$.

First, the evolution of the condition numbers for the HDG global and local problems is reported, for different mesh sizes and different polynomial degrees of approximation. Figure 12 displays the maximum condition numbers κ^{glob} and κ^{loc} of the global and local problems, respectively, over the set of meshes under analysis. In both cases, a linear growth

$\mathcal{O}(k)$ of the condition numbers as a function of the polynomial degree of approximation k is observed. It is worth remarking that, although the condition number of the local problem increases for high-order approximations and achieves values of approximately 10^{11} for $k = 4$, the size of such problems is usually fairly small (see Table 1) and they can thus be efficiently treated using direct solvers. On the contrary, owing to the choice of Legendre basis functions for the face-based unknowns, the global condition number is maintained at lower values, also allowing for iterative solvers to be employed. Of course, suitable preconditioners tailored for matrices with HDG structure play a significant role in this context, see, e.g., [72, 73] and should be further studied in the framework of unfitted discretizations.

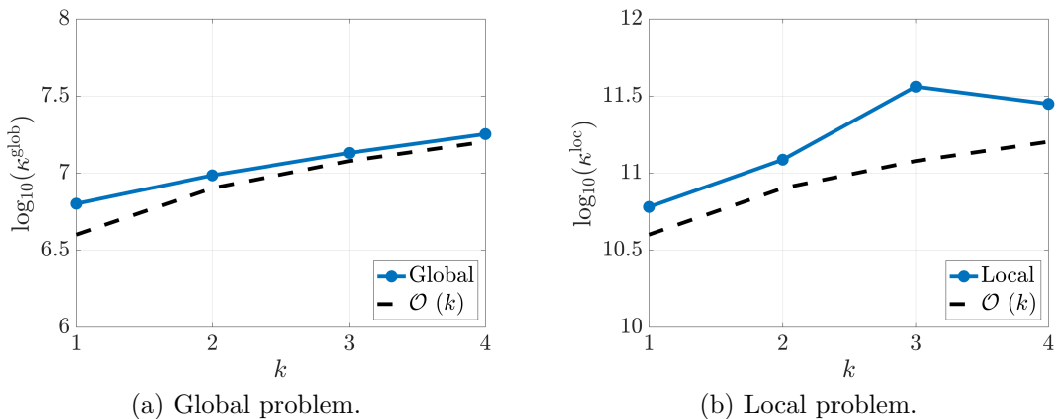


Figure 12: Taylor-Couette domain. Maximum value, over all the tested meshes, of the condition number of (a) the global problem and (b) the local problem as a function of the polynomial degree of approximation.

Table 1: Dimension of the local problems using square and hexahedra elements.

Order of interpolation	1	2	3	4	6	8	10
Standard HDG element / Immersed boundary element							
2D	29	64	113	176	344	568	848
3D	105	352	833	1 626	4 460	9 478	17 304
Interface element							
2D	57	127	225	351	687	1 135	1 695
3D	209	703	1 665	3 251	8 919	18 954	34 607

Remark 5 [HDG with Cauchy stress formulation] In many problems of engineering interest, the employment of the Cauchy stress formulation is preferred. Besides the modeling advantages related to Neumann conditions representing physical tensions (see, e.g., [70]), the choice of the strain rate tensor as point-wise symmetric HDG mixed variable using Voigt notation can also lead to a reduction of the

size of the local problems, by considering only the non-redundant components of \mathbf{L} [60, 74–77].

The evolution of the condition number κ^{glob} of the HDG global problem in terms of the local mesh size h is presented in Figure 13, for different polynomial degrees of approximations. The results display that the optimal rate $\mathcal{O}(h^{-2})$ for second-order elliptic differential operators is achieved for $h \rightarrow 0$.

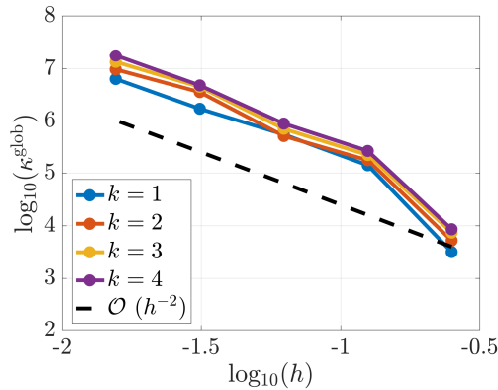


Figure 13: Taylor-Couette domain. Condition number of the global problem as a function of the local mesh size, for different polynomial degrees of approximation.

Finally, Figure 14 displays the convergence of the error, measured in the $\mathcal{L}^2(\Omega)$ norm, for pressure, gradient of velocity, primal and postprocessed velocities for different mesh sizes h and different polynomial degrees k . The results show optimal convergence of order $k + 1$ for p , \mathbf{L} and \mathbf{u} , as well as superconvergence of order $k + 2$ for \mathbf{u}_* . It is worth noticing that the obtained optimal convergence rates confirm the robustness of the proposed unfitted HDG methodology coupling the exact treatment of the boundary geometry according to the NEFEM rationale with the previously discussed element extension procedure, leading to a high-order immersed boundary method, without any loss of accuracy.

5.3 Unfitted interface of a circular bubble at equilibrium

In this section, a two-fluid problem is considered, with an unfitted interface describing a circular bubble Ω^1 , of radius $R=1/3$ centered in $(0.5, 0.5)$, immersed in an external fluid Ω^2 . The two fluids are assumed to be immiscible, with viscosity $\mu^1=10$ and $\mu^2=1$, respectively. The computational domain is defined as $\Omega_o=(0, 1)^2$ and an 8×8 mesh of square elements is constructed, with an appropriate element extension procedure to handle small cut cells (Figure 15).

Under the assumption of zero body forces (i.e., $\mathbf{s}=\mathbf{0}$) and no-slip boundary conditions

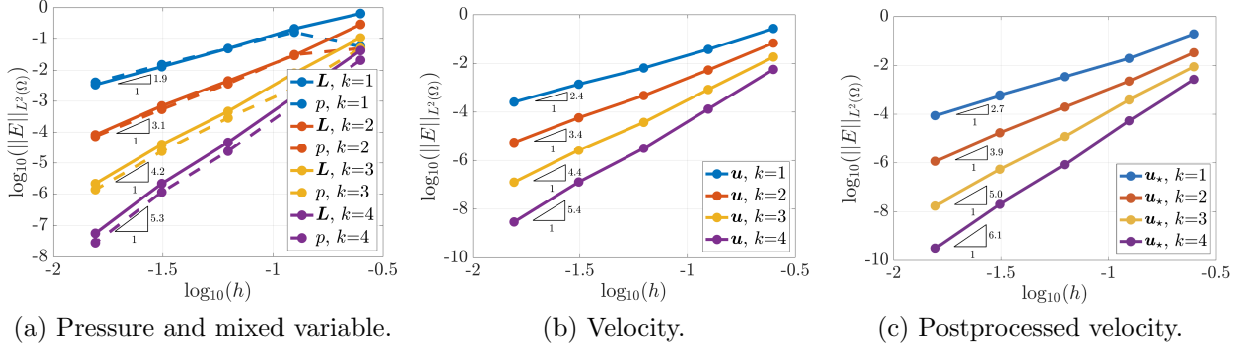


Figure 14: Taylor-Couette domain. Convergence of the error, measured in the $\mathcal{L}^2(\Omega)$ norm, as a function of the local mesh size h for (a) pressure (dashed lines) and mixed variable (continuous line), (b) velocity and (c) postprocessed velocity for different degrees of approximation $k = 1, \dots, 4$.

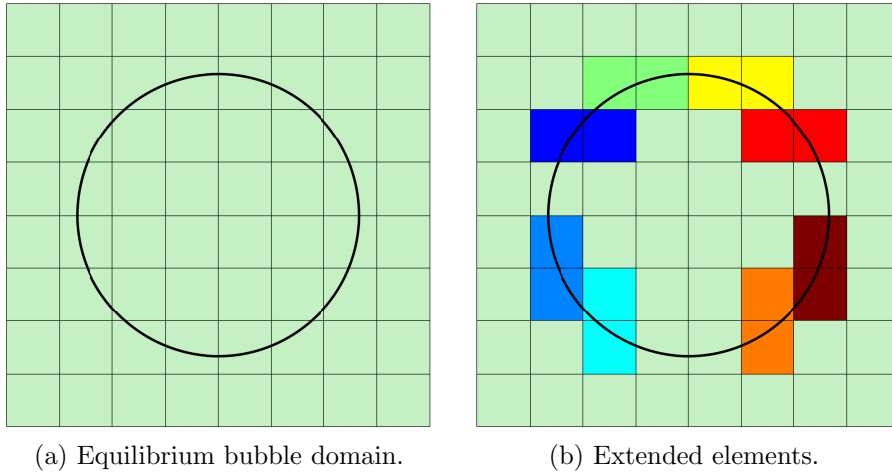


Figure 15: Equilibrium bubble domain and extension procedure to treat badly cut cells.

$\mathbf{u}_D = \mathbf{0}$ on $\partial\Omega_o$, the problem admits an analytical solution

$$\mathbf{u}^{\text{ref}} = \mathbf{0}, \quad p^{\text{ref}} = \begin{cases} \pi R \gamma - \frac{\gamma}{R}, & \text{if } r < R, \\ \pi R \gamma, & \text{elsewhere,} \end{cases}$$

with $\gamma=1$. It is worth noticing that the target velocity solution is constant in $\Omega^1 \cup \Omega^2$, whereas the target pressure is a discontinuous function, piecewise constant in Ω^1 and Ω^2 . Hence, the numerical results obtained using an HDG approximation of degree $k = 1$ yield a discretization error achieving machine precision for all variables, with errors measured in the $\mathcal{L}^2(\Omega_o)$ norm of order 10^{-12} for velocity, 10^{-9} for pressure and 10^{-10} for the gradient of velocity. Figure 16 reports a point-wise error map of the logarithm of the absolute error for the module of the velocity and the pressure, confirming the ability

of the method to accurately approximate the solution in the two fluid domains, while guaranteeing the equilibrium via the imposition of the transmission condition across the interface, geometrically described using a NURBS.

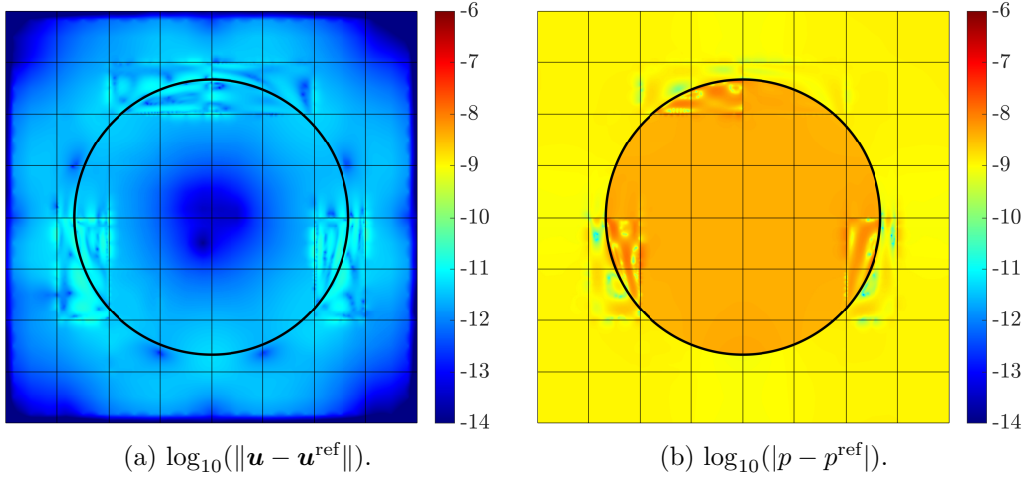


Figure 16: Equilibrium bubble domain. Logarithm of the point-wise absolute error of (a) the module of the velocity and (b) the pressure computed with polynomial functions of degree $k = 1$.

5.4 Microfluidic channel with complex unfitted obstacles

A microchannel inspired by the realistic design of a passive microfluidic mixer [78] is studied here to showcase the suitability of the unfitted HDG-NEFEM method to perform high-fidelity simulations of microfluidic flows in complex geometric systems described by NURBS. The microchannel Ω , displayed in Figure 17a, consists of a divergent-convergent structure with a series of eight circular obstacles located in the central portion of the domain. The geometric details of each inclusion (i.e., coordinates (x_c^i, y_c^i) of the centers and radii R^i of the circles) are reported in Table 2. A fluid with viscosity $\mu = 1$ enters from the top boundary (in blue), where the Dirichlet datum $\mathbf{u}_D = (0, -1)$ is imposed, and exits from the bottom contour (in red), where a homogeneous Neumann condition is applied. No-slip conditions are enforced on the remaining boundaries and on the obstacles to model physical walls. Moreover, body forces are set to zero.

The computational domain is defined as $\Omega_o = (0, 1)^2$ and it is subdivided into 32×32 square elements. It is worth noticing that given the rectangular shape of the domain Ω under analysis, approximately two thirds of the mesh elements are inactive lying in $\Omega_o \setminus \Omega$. Figure 17b displays the portion of Ω_o comprised in the region $(0.34375, 0.65625) \times (0, 1)$ and featuring 10×32 square elements, where Ω is located. In addition, the extended elements employed to avoid ill conditioning issues due to badly cut cells are reported in Figure 17c.

Table 2: Geometric data (coordinates (x_c^i, y_c^i) of the centers and radii R^i) of the eight circular obstacles, ordered from left to right.

Obstacle i		1	2	3	4	5	6	7	8
Center coordinate x_c^i	$[\times 10^{-1}]$	4.10	4.60	4.82	5.00	5.00	5.45	5.73	6.30
Center coordinate y_c^i	$[\times 10^{-1}]$	4.38	4.52	4.77	5.10	5.60	5.60	5.85	5.80
Radius R^i	$[\times 10^{-2}]$	3.4	1.2	1.2	2.0	2.5	1.5	2.0	3.0

Figure 18 shows pressure and velocity fields computed using the unfitted HDG-NEFEM method. While both fields appear smooth, the presence of the obstacles is responsible for a significant deviation of the flow, with a high pressure gradient (Figure 18a) and an acceleration of the flow (Figure 18b) in the vicinity of the left-most obstacle. In addition, the streamlines in Figure 18c clearly highlight an additional difficulty of this problem, with localized flow features appearing when two obstacles are not perfectly in contact.

To accurately describe the flow variations observed in [78] in the region featuring the obstacles, the degree adaptive procedure described in Section 3.3 is employed. Exploiting the superconvergence properties of HDG approximations in elliptic problems, the map of non-uniform polynomial degrees in Figure 18d is devised to ensure an accuracy of two significant digits in the velocity field. More precisely, the methodology automatically selects the most appropriate polynomial degree to locally approximate the flow, achieving degree 6 in the regions where very small features appear, while maintaining degree 1 and 2 where the flow is less complex. The map of the adapted degree in the vicinity of the obstacles, together with the extended elements employed for computation are reported in Figures 19a and 19b, respectively.

This confirms the ability of the method to provide highly accurate results, going high-order with the polynomial approximations, while limiting the increase of the computational cost. In addition, the adaptive procedure is capable of identifying the regions where physically relevant phenomena take place and automatically devising the precision required by the discretization. Finally, it is worth remarking that the combined use of unfitted meshes and exact description of the geometry via NURBS allows to achieve these results on relatively coarse meshes, whose design is not constrained by the geometric features of the domain. Moreover, the presented framework is robust also in the presence of elements cut in multiple subregions.

5.5 Multiple unfitted interfaces in an emulsion of two fluids

The last example features a two-fluid system describing an emulsion in a porous medium, with a downward flow due to the gravitational force as presented in [79–81]. More precisely, a dispersed phase referred to as fluid 1 (e.g., oil droplets) is immersed in a continuous phase

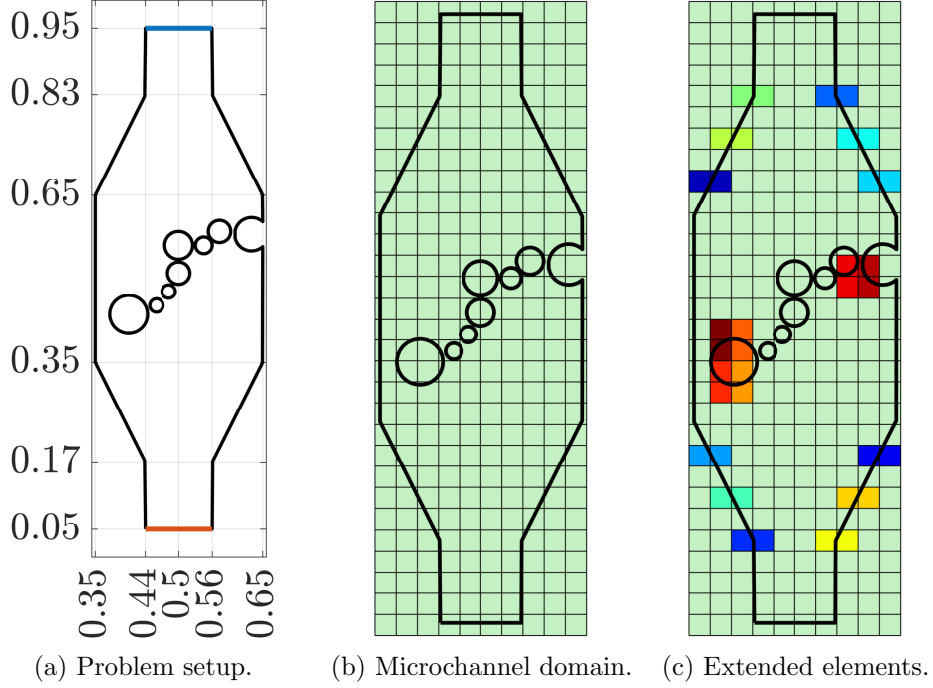


Figure 17: Microchannel domain. (a) Problem setup with physical walls (black), inlet (blue) and outlet (red) boundaries. (b) Detail of the computational domain in the region $(0.34375, 0.65625) \times (0, 1)$. (c) Element extension to avoid badly cut cells.

of the second fluid (e.g., water) that permeates the pores of a homogeneous porous medium.

Under the assumption of periodic porous medium, a microscopic unit cell $\Omega_o = (0, 1)^2$, illustrated in Figure 20a, is considered as computational domain, with a mesh of 32×32 square elements (Figure 20b). Upon a non-dimensional analysis of the physical data reported in [79–81], the following setup is employed. The solid matrix of the porous medium is defined as the brown circular region centered in $(0.5, 0.5)$ with radius $R_p = 0.25231$. This is assumed to be rigid and impermeable, leading to a material with porosity of approximately 0.8. The domain Ω^1 of fluid 1 is subdivided into 28 circular droplets, each defined by closed NURBS curves, whose geometric data are detailed in table 3. Fluid 2 is defined in the domain $\Omega^2 := \Omega_o \setminus \Omega^1$. A viscosity ratio $\mu^1/\mu^2 = 10$ is considered, with the viscosities of the two fluids being $\mu^1 = 40$ and $\mu^2 = 4$, respectively. To model the effect of gravity, the body force is set to $\mathbf{s} = (0, -613.125)$, whereas the surface tension coefficient $\gamma = 2.4 \times 10^5$ is employed to enforce the interface conditions between the two fluids. Finally, no-slip boundary conditions are imposed on the contour of the central pore $\{(x, y) \in \Omega_o : (x - 0.5)^2 + (y - 0.5)^2 = R_p^2\}$ and periodic conditions are prescribed on the top and bottom, as well as left and right boundaries of $\partial\Omega_o$.

Remark 6 [Periodic boundary conditions in HDG] Let Γ_L and Γ_R respectively denote the left and right vertical boundaries where periodic conditions are pre-

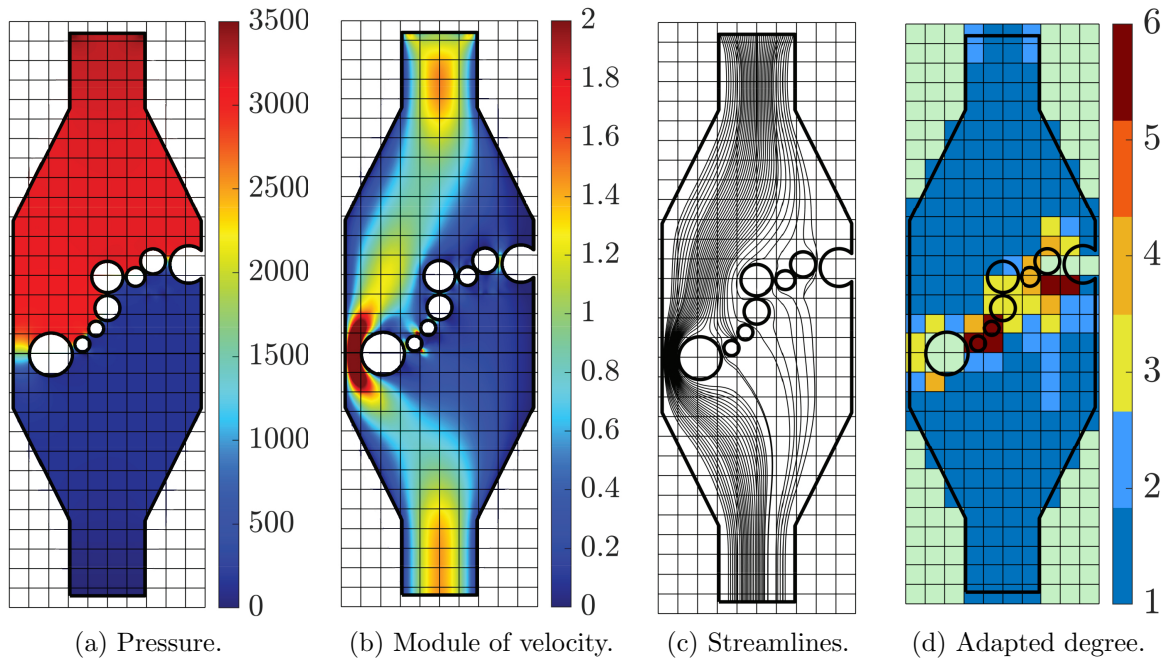


Figure 18: Microchannel domain. (a) Pressure. (b) Module of velocity. (c) Streamlines. (d) Map of the adapted polynomial degree of approximation.

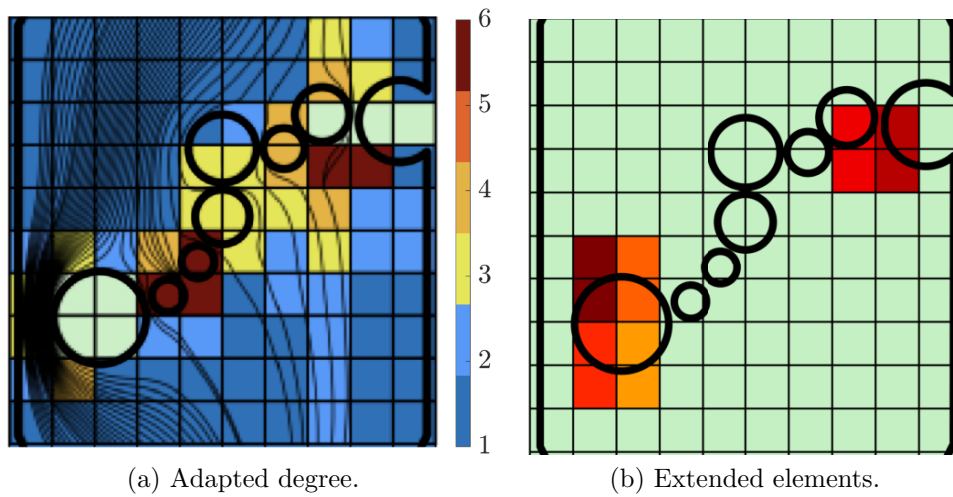


Figure 19: Microchannel domain. Detail of (a) the adapted degree superimposed with the streamlines and (b) the extended elements in the vicinity of the obstacles.

scribed. Assuming that the vertical coordinate of the nodes along Γ_L and Γ_R coincides, the imposition of periodic conditions in HDG methods is straightforward. By eliminating the hybrid unknown defined along Γ_R , the faces along Γ_L can be considered as internal faces, shared by the left-most and right-most elements. Thus,

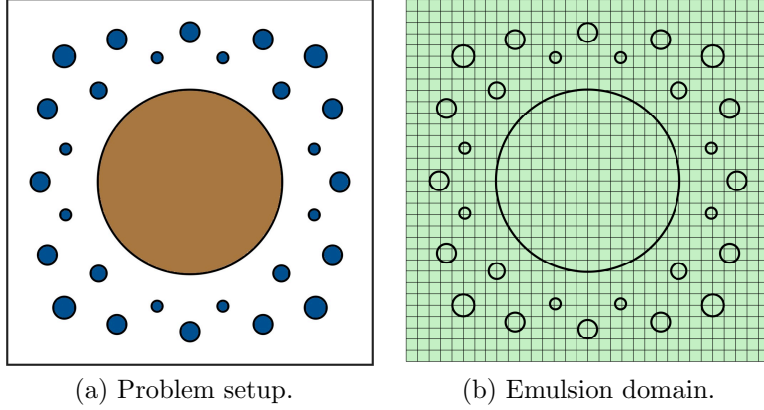


Figure 20: Emulsion domain. (a) Problem setup with fluid 1 (blue), fluid 2 (white) and solid pore (brown). (b) Computational domain.

Table 3: Geometric data (center coordinates (x_c^i, y_c^i) and radius R^i) of the 28 circular droplets.

Droplet i		1	2	3	4	5	6	7	8	9	10
Coord. x_c^i	$[\times 10^{-1}]$	1.56	1.56	8.44	8.44	5.0	1.0	5.0	9.0	7.0	3.0
Coord. y_c^i	$[\times 10^{-1}]$	1.56	8.44	8.44	1.56	1.0	5.0	9.0	5.0	1.1	1.1
Radius R^i	$[\times 10^{-2}]$	3.0	3.0	3.0	3.0	2.6	2.6	2.6	2.6	2.6	2.6
Droplet i		11	12	13	14	15	16	17	18	19	20
Coord. x_c^i	$[\times 10^{-1}]$	1.1	1.1	3.0	7.0	8.9	8.9	7.5	2.5	2.5	7.5
Coord. y_c^i	$[\times 10^{-1}]$	3.0	7.0	8.9	8.9	7.0	3.0	2.5	2.5	7.5	7.5
Radius R^i	$[\times 10^{-2}]$	2.6	2.6	2.6	2.6	2.6	2.6	2.2	2.2	2.2	2.2
Droplet i		21	22	23	24	25	26	27	28		
Coord. x_c^i	$[\times 10^{-1}]$	5.9	4.1	1.6	1.6	4.1	5.9	8.4	8.4		
Coord. y_c^i	$[\times 10^{-1}]$	1.6	1.6	4.1	5.9	8.4	8.4	4.1	5.9		
Radius R^i	$[\times 10^{-2}]$	1.5	1.5	1.5	1.5	1.5	1.5	1.5	1.5		

the matching of the solution along Γ_L and Γ_R follows automatically from the uniqueness of the hybrid variable along Γ_L . The equality of the fluxes across Γ_L and Γ_R is naturally enforced by means of the HDG global problem since the faces along Γ_L are now considered as internal faces. Of course, the above considerations can be extended to any pair of appropriately oriented boundaries Γ_I and Γ_J .

Figure 21 displays the pressure and velocity fields computed using the unfitted HDG approach, with a non-uniform polynomial degree approximation. The results show localized pressure jumps at the interfaces between fluid 1 and fluid 2. These are due to the effect of the surface tension, which depends upon the curvature of the droplets in the dis-

persed phase. More precisely, the pressure jump increases proportionally to the inverse of the radius of the droplets (Figure 21c). As commented for the previous cases, the element

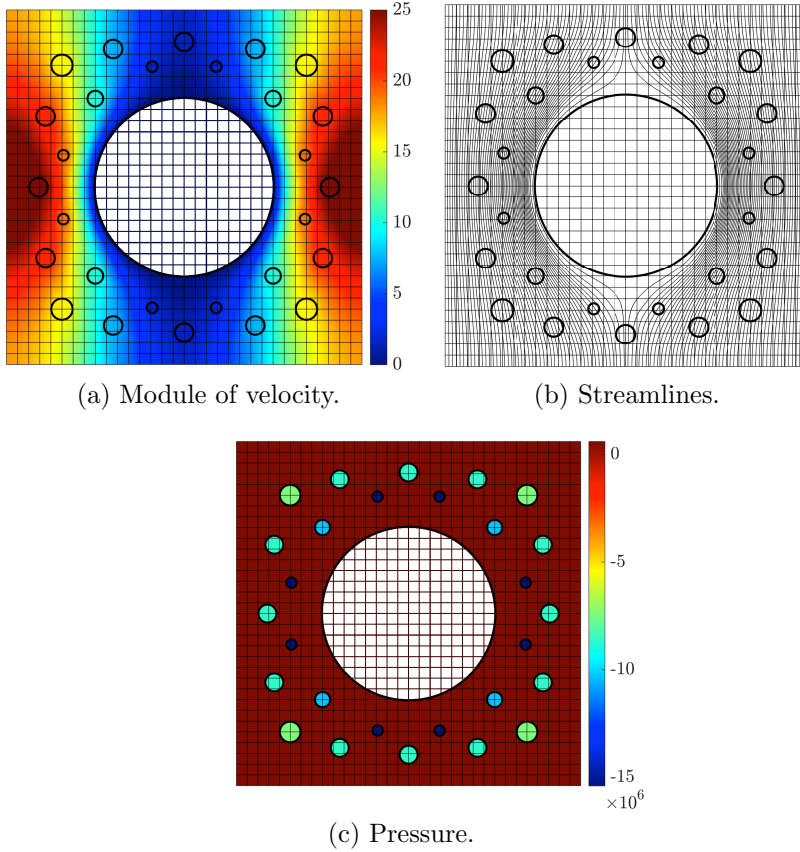


Figure 21: Emulsion domain. (a) Module of velocity. (b) Streamlines. (c) Pressure.

extension procedure is performed to avoid ill conditioning issues due to badly cut cells (Figure 22a). Moreover, the degree-adaptive procedure is employed to ensure two significant digits in the velocity approximation, yielding the map of adapted degrees in Figure 22b. The results show that the highest polynomial degree $k = 4$ is achieved in the vicinity of the central pore and, specifically, for the smallest droplets, whereas low-order polynomial functions are sufficient to accurately capture the solution away from the interfaces between fluid 1 and fluid 2. Hence, the combination of high-order functional approximation and exact description of the geometry via NURBS is also applicable to multi-fluid systems, with the unfitted framework allowing to bypass the difficulties of generating high-order curved meshes.

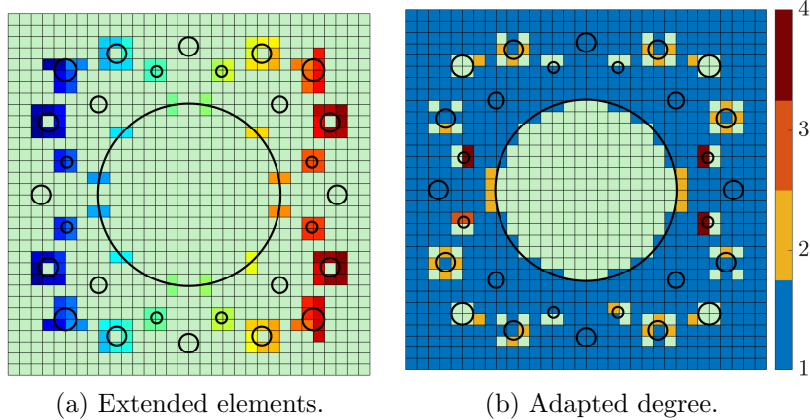


Figure 22: Emulsion domain. (a) Element extension to avoid badly cut cells. (b) Map of the adapted polynomial degree of approximation.

6 Concluding remarks

In this article, an unfitted high-order HDG method capable of treating exact geometries was presented. The method was successfully applied to incompressible one-fluid and two-fluid systems, with boundaries and interfaces described by means of NURBS, showcasing optimal high-order convergence and robustness even in the presence of badly cut cells or faces.

The non-conforming nature of this approach allows to achieve high-fidelity solutions, circumventing the generation of fitted, high-order, curved meshes. To this end, the method embeds the NURBS in a fixed Cartesian grid and an algorithm to intersect the NURBS with the mesh skeleton is executed. Note that this is trivial in 2D, whereas extension to 3D is more cumbersome, but doable using standard CAD tools.

Once the sets of cut elements and cut faces are identified, the unfitted HDG formulation only requires the appropriate integration of the equations in the physical domains for both element-based and face-based unknowns. On the one hand, uncut elements are treated as classic elements in standard HDG formulations. On the other hand, *immersed* elements cut by an unfitted boundary and *interface* elements featuring two fluids require special treatment: integration along immersed NURBS and integration in elements cut by a set of NURBS curves are accurately performed following the NEFEM rationale. In addition, to appropriately handle interface conditions, the method duplicates the unknowns in the mesh elements and on the mesh faces cut by the interface, thus enriching the approximation space to achieve a more precise discretization.

Hence, by combining non-conforming meshes, exact NURBS geometry and high-order degree-adaptive approximations, the presented unfitted HDG method provides accurate results on coarse meshes, which are independent of the geometric features of the domain.

Moreover, the use of coarse meshes minimizes the number of intersections between the mesh skeleton and the boundaries/interfaces, consequently reducing the computational overhead due to cut elements. Finally, the resulting unfitted HDG-NEFEM scheme does not introduce any new unknown on non-matching boundaries or interfaces, always solving for the global unknowns defined on the grid skeleton and preserving the favorable matrix structure of standard HDG methods.

Acknowledgements

This work was supported by the Spanish Ministry of Science and Innovation and the Spanish State Research Agency MCIN/AEI/10.13039/501100011033 (PID2020-113463RB-C33 to MG, PID2020-113463RB-C32 to AH, CEX2018-000797-S to MG and AH) and the Generalitat de Catalunya (2021-SGR-01049). MG is Fellow of the Serra Húnter Programme of the Generalitat de Catalunya.

References

- [1] S. Gross and A. Reusken. *Numerical methods for two-phase incompressible flows*, volume 40. Springer Science & Business Media, 2011.
- [2] Sergio Zlotnik and Pedro Díez. Hierarchical X-FEM for n -phase flow ($n > 2$). *Comput. Methods Appl. Mech. Eng.*, 198(30-32):2329–2338, 2009.
- [3] F. Heimann, C. Engwer, O. Ippisch, and P. Bastian. An unfitted interior penalty discontinuous Galerkin method for incompressible Navier-Stokes two-phase flow. *Int. J. Numer. Methods Fluids*, 71(3):269–293, 2013.
- [4] Z. J. Wang, Krzysztof Fidkowski, Rémi Abgrall, Francesco Bassi, Doru Caraeni, Andrew Cary, Herman Deconinck, Ralf Hartmann, Koen Hillewaert, H. T. Huynh, Norbert Kroll, Georg May, Per-Olof Persson, Bram van Leer, and Miguel Visbal. High-order CFD methods: current status and perspective. *Int. J. Numer. Methods Fluids*, 72(8):811–845, jan 2013.
- [5] M. S. Fabien, M. G. Knepley, and B. M. Rivière. A hybridizable discontinuous Galerkin method for two-phase flow in heterogeneous porous media. *Int. J. Numer. Methods Eng.*, 116(3):161–177, 2018.
- [6] A. Costa-Solé, E. Ruiz-Gironés, and J. Sarrate. An HDG formulation for incompressible and immiscible two-phase porous media flow problems. *Int. J. Comput. Fluid Dyn.*, 33(4):137–148, 2019.

- [7] R. Kirby, S. J. Sherwin, and B. Cockburn. To CG or to HDG: A comparative study. *J. Sci. Comput.*, 51(1):183–212, 2011.
- [8] Antonio Huerta, Aleksandar Angeloski, Xevi Roca, and Jaime Peraire. Efficiency of high-order elements for continuous and discontinuous Galerkin methods. *Int. J. Numer. Methods Eng.*, 96(9):529–560, 2013.
- [9] M. Woopen, A. Balan, G. May, and J. Schütz. A comparison of hybridized and standard DG methods for target-based *hp*-adaptive simulation of compressible flow. *Comput. Fluids*, 98:3 – 16, 2014.
- [10] F. Bassi and S. Rebay. High-order accurate discontinuous finite element solution of the 2D Euler equations. *J. Comput. Phys.*, 138(2):251–285, 1997.
- [11] R. Sevilla, S. Fernández-Méndez, and A. Huerta. NURBS-enhanced finite element method for Euler equations. *Int. J. Numer. Methods Fluids*, 57(9):1051–1069, 2008.
- [12] R. Sevilla, S. Fernández-Méndez, and A. Huerta. NURBS-enhanced finite element method (NEFEM). *Int. J. Numer. Methods Eng.*, 76(1):56–83, 2008.
- [13] R. Sevilla, S. Fernández-Méndez, and A. Huerta. 3D NURBS-enhanced finite element method (NEFEM). *Int. J. Numer. Methods Eng.*, 88(2):103–125, 2011.
- [14] R. Sevilla, L. Rees, and O. Hassan. The generation of triangular meshes for NURBS-enhanced FEM. *Int. J. Numer. Methods Eng.*, 108(8):941–968, 2016.
- [15] X. Zou, S.B. Lo, R. Sevilla, O. Hassan, and K. Morgan. The generation of 3D surface meshes for NURBS-Enhanced FEM. *Comput. Aided Des.*, page 103653, 2023.
- [16] R. Mittal and G. Iaccarino. Immersed boundary methods. *Annu. Rev. Fluid Mech.*, 37:239–261, 2005.
- [17] John W. Barrett and Charles M. Elliott. Fitted and unfitted finite-element methods for elliptic equations with smooth interfaces. *IMA J. Numer. Anal.*, 7(3):283–300, 1987.
- [18] Anita Hansbo and Peter Hansbo. An unfitted finite element method, based on Nitsche’s method for elliptic interface problems. *Comput. Methods Appl. Mech. Eng.*, 191(47-48):5537–5552, 2002.
- [19] Anita Hansbo and Peter Hansbo. A finite element method for the simulation of strong and weak discontinuities in solid mechanics. *Comput. Methods Appl. Mech. Eng.*, 193(33-35):3523–3540, 2004.
- [20] Roland Glowinski, Tsorng-Whay Pan, and Jacques Periaux. A fictitious domain method for Dirichlet problem and applications. *Comput. Methods Appl. Mech. Eng.*, 111(3-4):283–303, 1994.

- [21] Roland Glowinski, Tsorng-Whay Pan, and Jacques Periaux. A fictitious domain method for external incompressible viscous flow modeled by Navier-Stokes equations. *Comput. Methods Appl. Mech. Eng.*, 112(1-4):133–148, 1994.
- [22] Erik Burman and Peter Hansbo. Fictitious domain finite element methods using cut elements: I. A stabilized Lagrange multiplier method. *Comput. Methods Appl. Mech. Eng.*, 199(41-44):2680–2686, 2010.
- [23] Erik Burman and Peter Hansbo. Fictitious domain finite element methods using cut elements: II. A stabilized Nitsche method. *Appl. Numer. Math.*, 62(4):328–341, 2012.
- [24] Erik Burman, Susanne Claus, Peter Hansbo, Mats G. Larson, and Andre Massing. CutFEM: Discretizing geometry and partial differential equations. *Int. J. Numer. Methods Eng.*, 104(7):472–501, 2015.
- [25] C. Gürkan and A. Massing. A stabilized cut discontinuous Galerkin framework for elliptic boundary value and interface problems. *Comput. Methods Appl. Mech. Eng.*, 348:466–499, 2019.
- [26] J. Parvizian, A. Düster, and E. Rank. Finite cell method: h-and p-extension for embedded domain problems in solid mechanics. *Comput. Mech.*, 41(1):121–133, 2007.
- [27] S. Badia, F. Verdugo, and A.F. Martin. The aggregated unfitted finite element method for elliptic problems. *Comput. Methods Appl. Mech. Eng.*, 336:533–553, 2018.
- [28] Alex Main and Guglielmo Scovazzi. The shifted boundary method for embedded domain computations. Part I: Poisson and Stokes problems. *J. Comput. Phys.*, 372:972–995, 2018.
- [29] F. de Prenter, C.V. Verhoosel, G.J. van Zwieten, and E.H. van Brummelen. Condition number analysis and preconditioning of the finite cell method. *Comput. Methods Appl. Mech. Eng.*, 316:297–327, 2017.
- [30] Erik Burman. Ghost penalty. *C. R. Math.*, 348(21-22):1217–1220, 2010.
- [31] August Johansson and Mats G. Larson. A high order discontinuous Galerkin Nitsche method for elliptic problems with fictitious boundary. *Numer. Math.*, 123(4):607–628, 2013.
- [32] Héctor Navarro-García, Rubén Sevilla, Enrique Nadal, and Juan José Ródenas. High-order discontinuous Galerkin method for time-domain electromagnetics on geometry-independent Cartesian meshes. *Int. J. Numer. Methods Eng.*, 122(24):7632–7663, 2021.
- [33] E. Burman, S. Claus, P. Hansbo, M.G. Larson, and A. Massing. CutFEM: discretizing geometry and partial differential equations. *Int. J. Numer. Methods Eng.*, 104(7):472–501, 2015.

- [34] F. de Prenter, C.V. Verhoosel, E.H. van Brummelen, M.G. Larson, and S. Badia. Stability and conditioning of immersed finite element methods: analysis and remedies. *Arch. Comput. Methods Eng.*, pages 1–40, 2023.
- [35] D. Schillinger and M. Ruess. The Finite Cell Method: A review in the context of higher-order structural analysis of CAD and image-based geometric models. *Arch. Comput. Methods Eng.*, 22:391–455, 2015.
- [36] Christoph Lehrenfeld. High order unfitted finite element methods on level set domains using isoparametric mappings. *Comput. Methods Appl. Mech. Eng.*, 300:716–733, 2016.
- [37] B. Müller, S. Krämer-Eis, F. Kummer, and M. Oberlack. A high-order discontinuous Galerkin method for compressible flows with immersed boundaries. *Int. J. Numer. Methods Eng.*, 110(1):3–30, 2017.
- [38] M.G. Larson and S. Zahedi. Stabilization of high order cut finite element methods on surfaces. *IMA J. Numer. Anal.*, 40(3):1702–1745, 2020.
- [39] N.M. Atallah, C. Canuto, and G. Scovazzi. The high-order Shifted Boundary Method and its analysis. *Comput. Methods Appl. Mech. Eng.*, 394:114885, 2022.
- [40] S. Badia, E. Neiva, and F. Verdugo. Robust high-order unfitted finite elements by interpolation-based discrete extension. *Comput. Math. Appl.*, 127:105–126, 2022.
- [41] D. Schillinger and E. Rank. An unfitted hp-adaptive finite element method based on hierarchical B-splines for interface problems of complex geometry. *Comput. Methods Appl. Mech. Eng.*, 200(47-48):3358–3380, 2011.
- [42] M. Ruess, D. Schillinger, Y. Bazilevs, V. Varduhn, and E. Rank. Weakly enforced essential boundary conditions for NURBS-embedded and trimmed NURBS geometries on the basis of the finite cell method. *Int. J. Numer. Methods Eng.*, 95(10):811–846, 2013.
- [43] Grégory Legrain. A NURBS enhanced extended finite element approach for unfitted CAD analysis. *Comput. Mech.*, 52(4):913–929, 2013.
- [44] D. Kamensky, M.-C. Hsu, D. Schillinger, J.A. Evans, A. Aggarwal, Y. Bazilevs, M.S. Sacks, and T.J.R. Hughes. An immersogeometric variational framework for fluid–structure interaction: Application to bioprosthetic heart valves. *Comput. Methods Appl. Mech. Eng.*, 284:1005–1053, 2015.
- [45] T. Hoang, C.V. Verhoosel, C.-Z. Qin, F. Auricchio, A. Reali, and E.H. van Brummelen. Skeleton-stabilized immersogeometric analysis for incompressible viscous flow problems. *Comput. Methods Appl. Mech. Eng.*, 344:421–450, 2019.

- [46] O. Marco, R. Sevilla, Y. Zhang, J.J. Rodenas, and M. Tur. Exact 3D boundary representation in finite element analysis based on Cartesian grids independent of the geometry. *Int. J. Numer. Methods Eng.*, 103(6):445–468, 2015.
- [47] Bernardo Cockburn, Jayadeep Gopalakrishnan, and Raytcho Lazarov. Unified hybridization of discontinuous Galerkin, mixed, and continuous Galerkin methods for second order elliptic problems. *SIAM J. Numer. Anal.*, 47(2):1319–1365, 2009.
- [48] L. Piegl and W. Tiller. *The NURBS Book*. Monographs in Visual Communication. Springer Berlin, Heidelberg, 1995.
- [49] Ruben Sevilla and Antonio Huerta. HDG-NEFEM with degree adaptivity for Stokes flows. *J. Sci. Comput.*, 77(3):1953–1980, 2018.
- [50] H. Dong, B. Wang, Z. Xie, and L.-L. Wang. An unfitted hybridizable discontinuous Galerkin method for the Poisson interface problem and its error analysis. *IMA J. Numer. Anal.*, 37(1):444–476, 2016.
- [51] C. Gürkan, M. Kronbichler, and S. Fernández-Méndez. eXtended Hybridizable Discontinuous Galerkin with Heaviside enrichment for heat bimaterial problems. *J. Sci. Comput.*, 72(2):542–567, 2017.
- [52] C. Gürkan, M. Kronbichler, and S. Fernández-Méndez. eXtended hybridizable discontinuous Galerkin for incompressible flow problems with unfitted meshes and interfaces. *Int. J. Numer. Methods Eng.*, 117(7):756–777, 2019.
- [53] E. Burman, D. Elfverson, P. Hansbo, M.G. Larson, and K. Larsson. Hybridized CutFEM for elliptic interface problems. *SIAM J. Sci. Comput.*, 41(5):A3354–A3380, 2019.
- [54] E. Burman and A. Ern. An unfitted hybrid high-order method for elliptic interface problems. *SIAM J. Numer. Anal.*, 56(3):1525–1546, 2018.
- [55] Erik Burman, Matteo Cicuttin, Guillaume Delay, and Alexandre Ern. An unfitted hybrid high-order method with cell agglomeration for elliptic interface problems. *SIAM J. Sci. Comput.*, 43(2):A859–A882, 2021.
- [56] Erik Burman, Guillaume Delay, and Alexandre Ern. An unfitted hybrid high-order method for the Stokes interface problem. *IMA J. Numer. Anal.*, 41(4):2362–2387, 2021.
- [57] Stefano Piccardo and Alexandre Ern. Surface tension effects between two immiscible Stokes fluids: a computational study using unfitted hybrid high-order methods and a level-set scheme. *HAL*, 2023.
- [58] David F. Rogers. *An introduction to NURBS: with historical perspective*. Morgan Kaufmann Publishers Inc., San Francisco, CA, 2001.

- [59] Adeline Montlaur, Sonia Fernandez-Mendez, and Antonio Huerta. Discontinuous Galerkin methods for the Stokes equations using divergence-free approximations. *Int. J. Numer. Methods Fluids*, 57(9):1071–1092, 2008.
- [60] Matteo Giacomini, Ruben Sevilla, and Antonio Huerta. Tutorial on Hybridizable Discontinuous Galerkin (HDG) formulation for incompressible flow problems. In L. De Lorenzis and A. Düster, editors, *Modeling in Engineering Using Innovative Numerical Methods for Solids and Fluids*, volume 599 of *CISM International Centre for Mechanical Sciences*, pages 163–201. Springer International Publishing, 2020.
- [61] Ruben Sevilla and Antonio Huerta. Tutorial on Hybridizable Discontinuous Galerkin (HDG) for second-order elliptic problems. In J. Schröder and P. Wriggers, editors, *Advanced Finite Element Technologies*, volume 566 of *CISM International Centre for Mechanical Sciences*, pages 105–129. Springer International Publishing, 2016.
- [62] Matteo Giacomini, Ruben Sevilla, and Antonio Huerta. HDGlab: An Open-Source Implementation of the Hybridizable Discontinuous Galerkin Method in MATLAB. *Arch. Comput. Methods Eng.*, 28(3):1941–1986, 2021.
- [63] J. Nitsche. Über ein Variationsprinzip zur Lösung von Dirichlet-Problemen bei Verwendung von Teilräumen, die keinen Randbedingungen unterworfen sind. In *Abhandlungen aus dem mathematischen Seminar der Universität Hamburg*, volume 36, pages 9–15. Springer, 1971.
- [64] Douglas N Arnold, Franco Brezzi, Bernardo Cockburn, and L Donatella Marini. Unified analysis of discontinuous Galerkin methods for elliptic problems. *SIAM J. Numer. Anal.*, 39(5), 2002.
- [65] Ngoc Cuong Nguyen, Jaime Peraire, and Bernardo Cockburn. A hybridizable discontinuous Galerkin method for Stokes flow. *Comput. Methods Appl. Mech. Eng.*, 199(9-12):582–597, 2010.
- [66] Bernardo Cockburn, Jayadeep Gopalakrishnan, Ngoc Nguyen, Jaume Peraire, and Francisco-Javier Sayas. Analysis of HDG methods for Stokes flow. *Math. Comp.*, 80(274):723–760, 2011.
- [67] Giorgio Giorgiani, Sonia Fernández-Méndez, and Antonio Huerta. Hybridizable discontinuous Galerkin with degree adaptivity for the incompressible Navier–Stokes equations. *Comput. Fluids*, 98:196–208, 2014.
- [68] M. Giacomini and R. Sevilla. Discontinuous Galerkin approximations in computational mechanics: hybridization, exact geometry and degree adaptivity. *SN Appl. Sci.*, 1:1047, 2019.
- [69] Barry Joe and Richard B. Simpson. Corrections to Lee’s visibility polygon algorithm. *BIT Numer. Math.*, 27(4):458–473, 1987.

- [70] Jean Donea and Antonio Huerta. *Finite element methods for flow problems*. John Wiley & Sons, Chichester, 2003.
- [71] S. Badia, J. Droniou, and L. Yemm. Conditioning of a Hybrid High-Order Scheme on Meshes with Small Faces. *J. Sci. Comput.*, 92(2), 2022.
- [72] S. Rhebergen and G.N. Wells. Preconditioning of a hybridized discontinuous Galerkin finite element method for the Stokes equations. *J. Sci. Comput.*, 77(3):1936–1952, 2018.
- [73] S. Muralikrishnan, T. Bui-Thanh, and J. N. Shadid. A multilevel approach for trace system in HDG discretizations. *J. Comput. Phys.*, 407:109240, 2020.
- [74] R. Sevilla, M. Giacomini, A. Karkoulas, and A. Huerta. A superconvergent hybridisable discontinuous Galerkin method for linear elasticity. *Int. J. Numer. Methods Eng.*, 116(2):91–116, 2018.
- [75] Matteo Giacomini, Alexandros Karkoulas, Ruben Sevilla, and Antonio Huerta. A superconvergent HDG method for Stokes flow with strongly enforced symmetry of the stress tensor. *J. Sci. Comput.*, 77(3):1679–1702, 2018.
- [76] A. La Spina, M. Kronbichler, M. Giacomini, W. Wall, and A. Huerta. A weakly compressible hybridizable discontinuous Galerkin formulation for fluid-structure interaction problems. *Comput. Methods Appl. Mech. Eng.*, 372:113392, 2020.
- [77] Jordi Vila-Pérez, Matteo Giacomini, Ruben Sevilla, and Antonio Huerta. Hybridisable discontinuous Galerkin formulation of compressible flows. *Arch. Comput. Methods Eng.*, 28(2):753–784, 2021.
- [78] Junchao Wang, Naiyin Zhang, Jin Chen, Victor G. J. Rodgers, Philip Brisk, and William H. Grover. Finding the optimal design of a passive microfluidic mixer. *Lab Chip*, 19(21):3618–3627, 2019.
- [79] D.G. Avraam and A.C. Payatakes. Flow regimes and relative permeabilities during steady-state two-phase flow in porous media. *J. Fluid Mech.*, 293(2):207–236, 1995.
- [80] O.A. Luévano-Rivas and F.J. Valdés-Parada. Upscaling immiscible two-phase dispersed flow in homogeneous porous media: A mechanical equilibrium approach. *Chem. Eng. Sci.*, 126:116–131, 2015.
- [81] Emanuela Bianchi Janetti, Monica Riva, and Alberto Guadagnini. Effects of pore-scale geometry and wettability on two-phase relative permeabilities within elementary cells. *Water (Switzerland)*, 9(4), 2017.

A Identification of the intersections of NURBS curves with the computational mesh

In this appendix, the strategy to identify the intersection of a NURBS curve with the computational mesh Ω_o is briefly presented.

First, for each NURBS curve \mathbf{C}_{Υ}^j , $j = 1, \dots, \mathbf{n}_{\Upsilon}$ composing the interface Υ , a *sufficiently large* number (e.g., $n_j = 100$) of sampling points $\{\mathbf{x}_k^j\}_{k=1, \dots, n_j}$ is introduced to represent the NURBS. The points \mathbf{x}_k^j are set equispaced in the parametric NURBS domain $[0, 1]$, that is, $\mathbf{x}_k^j = \mathbf{C}_{\Upsilon}^j(\lambda_k^j)$, with $\lambda_k^j = k/n_j$, and $k = 0, \dots, n_j$.

For all $k = 0, \dots, n_j$ and all $j = 1, \dots, \mathbf{n}_{\Upsilon}$, the mesh element Ω_e containing \mathbf{x}_k^j is identified, thus providing the list of *cut elements*. Note that this strategy can be easily optimized, via parallelization or by means of efficient sequential algorithms searching for cut elements only in the neighborhood of already defined cut elements.

Once cut elements are identified, cut faces need to be determined. To this end, for each cut element Ω_e and all $k = 1, \dots, n_j - 1$, the procedure seeks the points \mathbf{x}_m^j , $m = k - 1, \dots, k + 1$, neighbors of \mathbf{x}_k^j , and lying outside of Ω_e . Given a point \mathbf{x}_m^j outside of Ω_e , owing to the continuity of \mathbf{C}^j , the intersection point $\bar{\mathbf{x}}_{e,n}^j = \mathbf{C}_{\Upsilon}^j(\lambda_n^j)$ between Υ and $\partial\Omega_e$ is determined via a dichotomy algorithm, with $\lambda_n^j \in [\lambda_{k-1}^j, \lambda_{k+1}^j]$.

Hence, the portion of the interface lying within the cut element is denoted by $\Upsilon_e = \Upsilon \cap \Omega_e$ and its intersections with $\partial\Omega_e$ are given by the points $\bar{\mathbf{x}}_{e,n}^j$, with $n = 1, 2$. Under the assumption that the interface does not intersect an element through a vertex, for any intersection points $\bar{\mathbf{x}}_{e,n}^j$, with $j = 1, \dots, \mathbf{n}_{\Upsilon}$ and $n = 1, 2$, between Υ and $\partial\Omega_e$, there exists a corresponding intersection point $\bar{\mathbf{x}}_{k,n}^j = \bar{\mathbf{x}}_{e,n}^j$, lying in a neighboring element Ω_k which shares a face with Ω_e . If this condition is not satisfied, a local refinement is performed to look for missing cut elements.

Remark 7 [NURBS sampling] The previously mentioned approximation of Υ using n_j sampling points is only employed to identify the intersections of the NURBS with the mesh skeleton. For the purpose of computation, integration is performed on the curved triangles, with boundary described by the exact NURBS curve, using the NEFEM rationale [12].

Remark 8 [Multiple unfitted regions] The above considerations for the identification of the intersections rely on the assumption that a cut element is divided, at most, in two regions. Consider now an element Ω_e with n_e^j intersection points between Υ and $\partial\Omega_e$, that is, $\bar{\mathbf{x}}_{e,n}^j$, with $n = 1, \dots, n_e^j$. Hence, the element Ω_e is split into $n_e^j/2 + 1$ disjoint regions and Υ_e is composed of $n_e^j - 1$ disjoint curves $\Upsilon_{e,\ell}$ such that

$$\Upsilon_e = \bigcup_{\ell=1}^{n_e^j-1} \Upsilon_{e,\ell},$$

where each curve $\Upsilon_{e,\ell}$ is continuous and can be composed of multiple NURBS curves \mathcal{C}_{Υ}^j . This leads to

$$\Upsilon_{e,\ell} = \bigcup_{j \in \mathcal{J}_{e,\ell}} \mathcal{C}_{\Upsilon}^j(\lambda), \quad \forall \lambda \in [0, 1],$$

with $\mathcal{J}_{e,\ell}$ being the set of coefficients j of the NURBS curves \mathcal{C}_{Υ}^j describing the portion $\Upsilon_{e,\ell}$ of the interface.

B Triangulation procedure for quadrature involving an element cut by NURBS curves

In this appendix, the quadrature procedure for an element Ω_e , cut by a NURBS curve Υ_e , is presented. Given a cut element, quadrature is performed following the NEFEM rationale [14]. More precisely, for each region Ω_e^i , a triangulation is constructed, as sketched in Figure 23.

First, the region Ω_e^i is identified (Figure 23a) according to the procedure presented in Section 4.1. This region is described by the vertices of Ω_e lying in Ω_e^i (green vertices), the extrema of Υ_e^j , with $j = 1, \dots, n_{\Upsilon}$, intersecting $\partial\Omega_e$ (yellow points) and a set of points sampling the NURBS curves Υ_e^j . More precisely, in Figure 23a, the interface Υ_e is composed of two NURBS curves, split by the red point, and sampled at the locations of the six blue points. As a general rule, the number of sampling points along the NURBS is selected proportional to the inverse of the curvature of Υ_e , to accurately describe the curve.

Then, an initial point $\mathbf{x}_0 \in \Omega_e^i$ is selected (e.g., a vertex or the barycenter of a face belonging to $\partial\Omega_e^i$) to execute Lee's visibility algorithm [69]. In Figure 23b, the starting point is the bottom-left orange vertex. The goal of this procedure is to identify the subregions of Ω_e^i visible from \mathbf{x}_0 , that is, to determine all the sampling points that can be connected to \mathbf{x}_0 , without intersecting the NURBS curves Υ_e more than once. The visibility region is thus defined as the polygon delimited by \mathbf{x}_0 and all the visible points. In Figure 23b, the visibility region is identified by the orange vertex, the yellow point at the bottom and the red point.

The procedure is then repeated for the portion of the NURBS not yet explored. Following [14], the second starting point is selected as the mid-point between the last visible point (red point) and a vertex (top-left green point). Figure 23c assesses the visibility region starting from the orange point.

The procedure is iteratively repeated until Ω_e^i is completely partitioned into visible subregions, as reported in Figure 23d. The resulting triangles feature, at most, one curved edge, exactly describing the geometry of Υ_e by means of one NURBS curve. Generalizations of these results are discussed in [14]. Finally, it is worth recalling that this triangulation is only constructed to perform numerical quadrature on Ω_e^i , whereas the functional approximation is maintained in the original nodes of the underlying Cartesian grid.

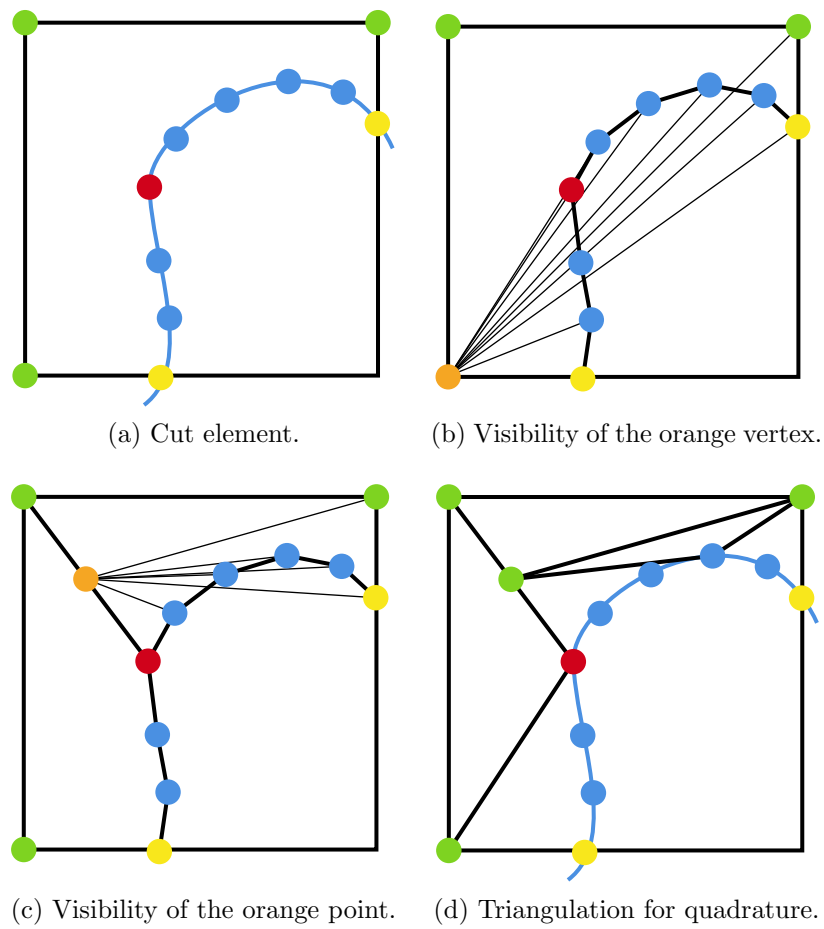


Figure 23: Triangulation procedure for a region Ω_e^i , within an element Ω_e cut by a NURBS curve Υ_e .